



Usher syndrome type 1-associated cadherins shape the photoreceptor outer segment

Cataldo Schietroma, Karine Parain, Amrit Estivalet, Asadollah Aghaie, Jacques Boutet de Monvel, Serge Picaud, José-Alain Sahel, Muriel Perron, Aziz El-Amraoui, Christine Petit

► To cite this version:

Cataldo Schietroma, Karine Parain, Amrit Estivalet, Asadollah Aghaie, Jacques Boutet de Monvel, et al.. Usher syndrome type 1-associated cadherins shape the photoreceptor outer segment. *Journal of Cell Biology*, 2017, 216 (6), pp.1849 - 1864. 10.1083/jcb.201612030 . pasteur-01534475

HAL Id: pasteur-01534475

<https://pasteur.hal.science/pasteur-01534475>

Submitted on 7 Jun 2017

HAL is a multi-disciplinary open access archive for the deposit and dissemination of scientific research documents, whether they are published or not. The documents may come from teaching and research institutions in France or abroad, or from public or private research centers.

L'archive ouverte pluridisciplinaire **HAL**, est destinée au dépôt et à la diffusion de documents scientifiques de niveau recherche, publiés ou non, émanant des établissements d'enseignement et de recherche français ou étrangers, des laboratoires publics ou privés.



Distributed under a Creative Commons Attribution - NonCommercial - ShareAlike 4.0 International License

Usher syndrome type 1-associated cadherins shape the photoreceptor outer segment

Cataldo Schietroma,^{1,2,3,4} Karine Parain,⁶ Amrit Estivalet,^{2,3,4} Asadollah Aghaie,^{2,3,4} Jacques Boutet de Monvel,^{1,2,3} Serge Picaud,^{3,5} José-Alain Sahel,^{3,5} Muriel Perron,^{6,7} Aziz El-Amraoui,^{1,2,3*} and Christine Petit^{1,2,3,4,8*}

¹Institut Pasteur, Génétique et Physiologie de l'Audition, 75015 Paris, France

²Institut National de la Santé et de la Recherche Médicale, Unité Mixte de Recherche-UMRS 1120, France

³Sorbonne Universités, UPMC University Paris, Complexité du Vivant, 75005 Paris, France

⁴Syndrome de Usher et Autres Atteintes Rétino-Cochlaires and ⁵Retinal information processing - Pharmacology and Pathology, Institut de la Vision, 75012 Paris, France

⁶Paris-Saclay Institute of Neuroscience, Centre National de la Recherche Scientifique, Université Paris Sud, Université Paris-Saclay, 91405 Orsay, France

⁷Centre d'Etude et de Recherche Thérapeutique en Ophtalmologie, Retina France, 94405 Orsay, France

⁸Collège de France, 75005 Paris, France

Usher syndrome type 1 (USH1) causes combined hearing and sight defects, but how mutations in USH1 genes lead to retinal dystrophy in patients remains elusive. The USH1 protein complex is associated with calyceal processes, which are microvilli of unknown function surrounding the base of the photoreceptor outer segment. We show that in *Xenopus tropicalis*, these processes are connected to the outer-segment membrane by links composed of protocadherin-15 (USH1F protein). Protocadherin-15 deficiency, obtained by a knockdown approach, leads to impaired photoreceptor function and abnormally shaped photoreceptor outer segments. Rod basal outer disks displayed excessive outgrowth, and cone outer segments were curved, with lamellae of heterogeneous sizes, defects also observed upon knockdown of *Cdh23*, encoding cadherin-23 (USH1D protein). The calyceal processes were virtually absent in cones and displayed markedly reduced F-actin content in rods, suggesting that protocadherin-15-containing links are essential for their development and/or maintenance. We propose that calyceal processes, together with their associated links, control the sizing of rod disks and cone lamellae throughout their daily renewal.

Introduction

Usher syndrome type 1 (USH1) is the major cause of combined, severe, inherited hearing and sight defects. It is characterized by profound congenital sensorineural deafness and retinitis pigmentosa of prepubertal onset leading to blindness (Richardson et al., 2011; El-Amraoui and Petit, 2014; Mathur and Yang, 2015). The six identified USH1 genes encode the transmembrane Ca^{2+} -dependent adhesion proteins protocadherin-15 and cadherin-23, the submembrane scaffold proteins harmonin and sans, the actin-based motor protein myosin VIIa, and the calcium- and integrin-binding protein CIB2 (Well et al., 1995; Bitner-Glindzicz et al., 2000; Verpy et al., 2000; Ahmed et al., 2001; Alagramam et al., 2001; Bolz et al., 2001; Bork et al., 2001; Weil et al., 2003; Riazuddin et al., 2012). In the sensory cells of the inner ear, the hair cells, USH1 proteins are present in the developing hair bundle, which forms their mechanosensory antenna (Richardson et al., 2011; Saieddine et al., 2012). The hair bundle is an array of stereocilia,

actin-filled microvilli, organized into rows of graded heights that develop under the morphogenetic control of a primary cilium, the kinocilium. Protocadherin-15 and cadherin-23 form transient, lateral links between growing stereocilia and between the kinocilium and the surrounding stereocilia, whereas harmonin, sans, and myosin VIIa anchor these links to the actin core of the stereocilia (Boëda et al., 2002; Siemens et al., 2002; Adato et al., 2005; Lagziel et al., 2005; Michel et al., 2005; Bahloul et al., 2010; Caberlotto et al., 2011). The USH1 proteins form a complex required for the cohesiveness of the stereocilia within the developing hair bundle (Lefèvre et al., 2008; Richardson et al., 2011). This complex thereafter has a key role in the mechanoelectrical transduction (MET) machinery, which converts the sound-evoked deflections of the hair bundle into electrical signals. Notably, protocadherin-15 and cadherin-23 form the tip-link, a fibrous link that gates the MET channels (Kazmierczak et al., 2007; Pepermans et al., 2014). Mutant mice lacking any of these proteins reproduce the USH1 hearing impairment. In contrast, unlike patients with USH1, these mice display no retinal degeneration (Williams, 2008; El-Amraoui and Petit, 2014). As a result, the functions of the USH1 protein com-

*A. El-Amraoui and C. Petit contributed equally to this paper.

Correspondence to Aziz El-Amraoui: aziz.el-amraoui@pasteur.fr; or Christine Petit: christine.petit@pasteur.fr

Abbreviations used: CCD, charge-coupled device; CI, confidence interval; dpf, days postfertilization; ERG, electroretinogram; $I_{0.5}$, half-saturating amplitude; K-S, Kolmogorov-Smirnov; LED, light-emitting diode; MET, mechanoelectrical transduction; MMR, Marc's modified ringer; MO, morpholino; RDS, retinal degeneration slow; RPE, retinal pigment epithelium; TEM, transmission electron microscopy; USH1, Usher syndrome type 1.

© 2017 Schietroma et al. This article is distributed under the terms of an Attribution-Noncommercial-Share Alike-No Mirror Sites license for the first six months after the publication date (see <http://www.rupress.org/terms/>). After six months it is available under a Creative Commons License (Attribution-Noncommercial-Share Alike 4.0 International license, as described at <https://creativecommons.org/licenses/by-nc-sa/4.0/>).



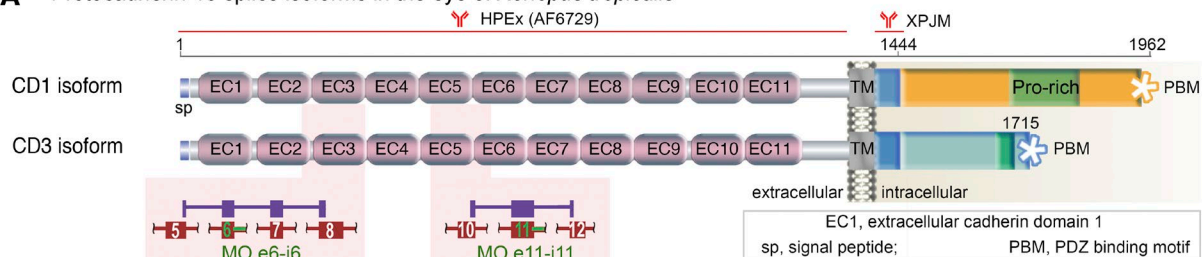
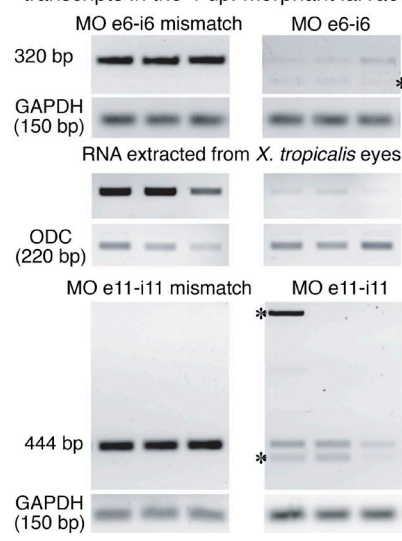
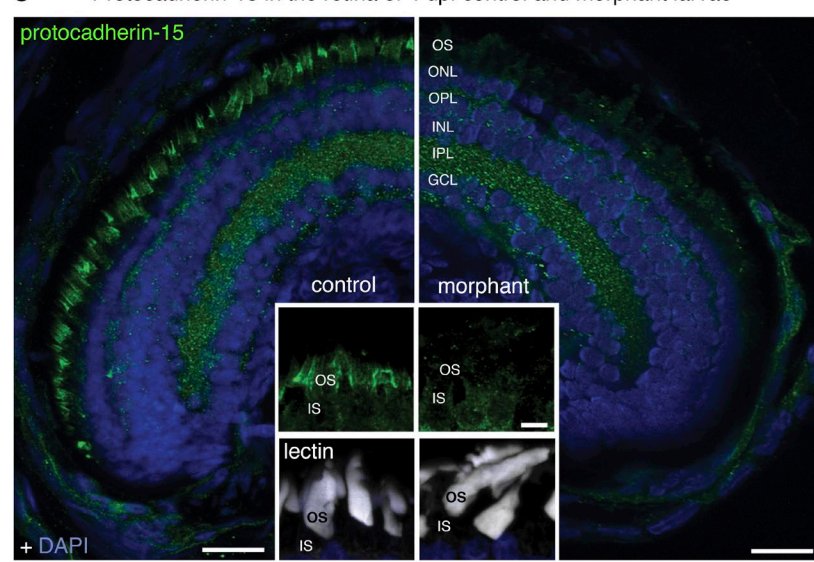
A Protocadherin-15 splice isoforms in the eye of *Xenopus tropicalis***B Aberrant splicing of *pcdh15* transcripts in the 4 dpf morphant larvae****C Protocadherin-15 in the retina of 4 dpf control and morphant larvae**

Figure 1. Antisense morpholino (MO) oligonucleotides block *pcdh15* expression in the retina of *X. tropicalis*. (A) Predicted domain structure of the two splice isoforms of *X. tropicalis* protocadherin-15, positions of the antibodies used in the study, and *pcdh15* MO e6-i6 and MO e11-i11. Aberrant splicing of *pcdh15* transcripts is predicted to result in premature stop codons. (B) MO e6-i6 and MO e11-i11 affect pre-mRNA splicing and lead to several abnormal RT-PCR products (asterisks) because of intron retention, exon skipping, and the use of alternative splice sites. The overall reduction in the amount of the RT-PCR products is probably because of the nonsense-mediated decay of incorrectly spliced mRNAs. Abnormal transcripts and nonsense-mediated decay were not detected in control larvae microinjected with five-base mismatch control oligonucleotide. Ornithine decarboxylase (ODC) and glyceraldehyde 3-phosphate dehydrogenase (GAPDH) mRNAs were used as loading controls. (C) Lower levels of photoreceptor labeling for protocadherin-15 (green) in the 4 dpf larva microinjected with MO e6-i6 (right) than in the 4-dpf larva treated with the mismatch oligonucleotide control. Cell nuclei were stained with DAPI (blue). Insets: details of the inner segment (IS)-outer segment (OS) interface, with fluorescent lectins (white) and protocadherin-15 (green) staining is shown. ONL, outer nuclear layer; OPL, outer plexiform layer; INL, inner nuclear layer; IPL, inner plexiform layer; GCL, ganglion cell layer. Bars: (main) 20 μ m; (insets) 5 μ m.

plex in the retina and the cellular mechanisms underlying the visual impairment of patients with USH1 remain elusive.

Previous studies in humans, nonhuman primates, and amphibians have revealed that all USH1 proteins are located at the calyceal processes of the photoreceptor cells (Sahly et al., 2012). These actin-filled processes emerge from the inner segment of the photoreceptor cell, the metabolic compartment of the photoreceptor, in which they are anchored by deep F-actin roots. They form a barrel-like structure enclosing the base of the outer segment in cones and rods, the compartment responsible for phototransduction (Szikra et al., 2014). The calyceal processes were described 60 yr ago (Sjöstrand and Elfvin, 1957; Cohen, 1963), but their function is unknown. Such a ring-like sheath of calyceal processes is absent from the photoreceptor cells of rodents, in which only very rare membrane protrusions emerge from the inner segment and extend along the outer segment (Sahly et al., 2012; Volland et al., 2015). This interspecies difference and the absence of USH1-like retinopathy in USH1 mutant mice highlight the need for alternative and more appropriate animal models to understand the role of the USH1 proteins in human retinas (Sahly et al., 2012).

Here, we addressed this issue by knocking down protocadherin-15 or cadherin-23 expression with a morpholino (MO)-based knockdown strategy in *Xenopus tropicalis*, which displays large photoreceptor cells with well-developed calyceal processes (Stiemke et al., 1994; Witkovsky, 2000). We show that protocadherin-15-containing links control the development and maintenance of the calyceal processes and demonstrate the crucial role these processes have in controlling the size of photoreceptor disks in rods and the lamellae in cones. We suggest that the calyceal processes exert a mechanical constraint on the base of the outer segment, which is required to oppose the deforming forces associated with its continuous renewal. These findings provide significant insights into the underlying mechanisms of the pathogenesis of USH1 retinal dystrophy.

Results

Inhibition of *pcdh15* or *cdh23* expression in *X. tropicalis*

We investigated the retinal function of USH1 genes in *X. tropicalis* rather than *Xenopus laevis*, because its diploid genome (Hirsch

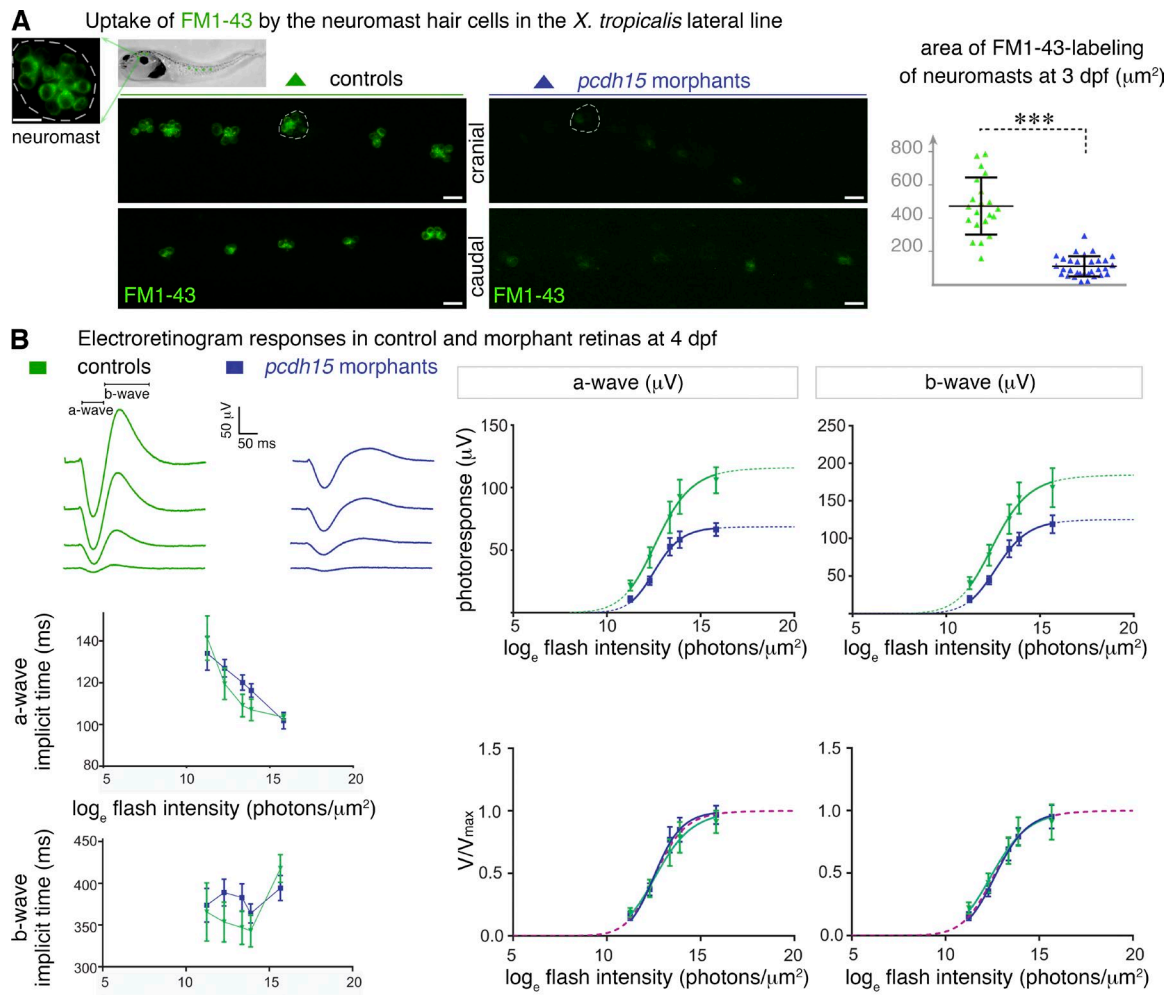


Figure 2. *Pcdh15* morphant larvae have altered mechanoelectrical transduction channels and photosensory deficits. (A) Uptake of FM1-43 dye by the hair cells of cranial and caudal neuromasts (high magnification of a neuromast, with 6–12 sensory hair cells shown). Dye uptake in neuromasts (some are outlined) is much weaker in 3-dpf *pcdh15* morphants than it is in controls: $120.6 \pm 15.5 \mu\text{m}^2$ in morphants (mean \pm SEM; $n = 33$), versus $471.2 \pm 37.5 \mu\text{m}^2$ in controls ($n = 21$; unpaired *t* test, *** $P < 0.0001$). (B, top left) Representative electroretinogram traces (flash intensity increasing from bottom to top). (bottom left) The time-to-peak values obtained for the a- and b-waves (implicit times) did not differ significantly between controls and morphants. (right) Photoreponse curves ($V, \mu\text{V}$), plotted as a function of flash intensity and fitted with the Naka-Rushton function, in morphants and controls. The responses show a significant attenuation in morphants (comparison of fits by the least-squares method: $P < 0.0001$ for both waves), whereas after normalization by the maximum value V_{\max} , they do not differ significantly, giving similar values of $I_{0.5}$ ($P > 0.5$ for both waves; bottom right panel; $n = 7$ controls, 13 morphants). Bars, 20 μm .

et al., 2002) makes the knockdown strategy easier. Several MO antisense oligonucleotides designed to block USH1 mRNA translation or pre-mRNA splicing were injected into *X. tropicalis* at the one- or two-cell stage (see Fig. S1). Developmental defects prevented reliable characterization of larvae receiving injections of MO targeting the expression of the harmonin, myosin VIIa, and sans genes (Fig. S1 A). We, therefore, focused on the genes encoding cadherin-23 (Fig. S1 B and Fig. S3, B and C) and protocadherin-15 (Fig. S1 C and Figs. 1, 2, 3, 4, 5, 6, 7, and 8).

We first analyzed *pcdh15* transcript levels in the larval eye by RT-PCR. We identified two different *pcdh15* transcripts, predicted to encode protocadherin-15 isoforms, with an extracellular region consisting of 11 cadherin-like (extracellular cadherin) repeats and a single transmembrane domain (Fig. 1 A), similar to the three protocadherin-15 isoforms (CD1–3) found in humans and mice (Alagramam et al., 2007). Sequence analysis indicated that the two *pcdh15* transcripts in *X. tropicalis* eyes encoded

CD1-like (accession no. KX463408) and CD3-like (accession no. KX463409) isoforms, each ending with an isoform-specific, C-terminal, class-I PDZ domain-binding motif (Fig. 1 A).

We used MOs targeting the intron splice sites abutting exons 6 (MO e6-i6) and 11 (MO e11-i11) to knockdown *pcdh15* expression (Fig. 1 A). The *X. tropicalis* larvae injected with MOs are hereafter referred to as morphants. Larvae injected with a five-base, mismatch oligonucleotide or with the standard control MO (see Materials and methods) were indistinguishable from non-treated embryos and were used as controls. Semiquantitative RT-PCR on total eye RNA showed that MO injection in *X. tropicalis* embryos resulted in abnormal mature transcripts and nonsense-mediated decay in the 4-d postfertilization (dpf) larvae. Sequencing of the amplicons confirmed the occurrence of exon skipping, intron retention, and alternative splicing (Fig. 1 B). The largest decrease in the levels of correctly spliced *pcdh15* mRNA ranged between 75 and 95% (95% confidence interval [95% CI]) and was obtained with MO

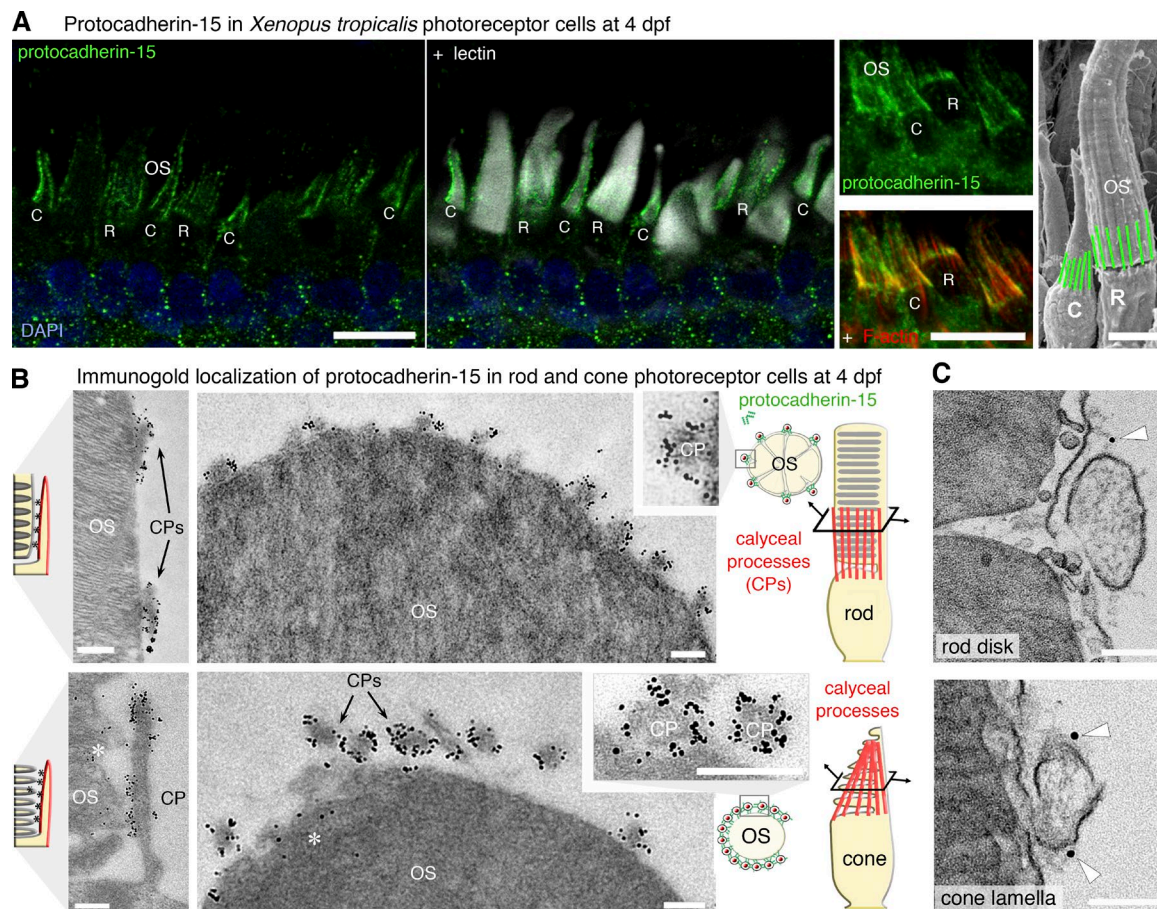


Figure 3. Protocadherin-15 is located at the calyceal processes of photoreceptor cells in *X. tropicalis* larvae. [A] In 4 dpf larvae, protocadherin-15 (green) is located around the base of the lectin-labeled (white) rod (R) and cone (C) outer segments (OS). Protocadherin-15 colocalizes with F-actin (red) that fill the calyceal processes (CPs). [B] In pre-embedding immunogold electron micrographs, silver-enhanced immunogold particles showed protocadherin-15 to be localized at the CPs surrounding the rod (top) and cone (bottom) OS. Sparse gold particles also decorate the lamellar membrane in cones (asterisks). [C] Protocadherin-15 immunolabeled gold particles (arrowheads) were localized with filaments connecting the CPs to the OS plasma membrane in rods (top) and cones (bottom). Bars: (A) 10 μ m; (A, SEM image) 5 μ m; (B) 200 nm; (C) 100 nm.

Downloaded from on June 2, 2017

e6-i6 (Fig. 1 B and Fig. S1 C). This MO was used in most of the experiments described here. A significant decrease in the amount of correctly spliced *pcdh15* mRNA (between 75 and 85%, 95% CI) was also obtained with MO e11-i11 (Fig. S1 C). The protocadherin-15 signal was almost undetectable at the photoreceptor cells of immunostained retinas in MO e6-i6 morphants (Fig. 1 C and Fig. S1 D) and was very weak in MO e11-i11 morphants (Fig. S1 D).

We extended our knockdown approach to *cdh23* morphants. The largest decrease in the abundance of correctly spliced *cdh23* mRNA ranged between 63 and 89% (95% CI) and was obtained with the *cdh23* MO targeting the splice donor site at the 3' end of exon 9, MO e9-i9 (Fig. S3 C).

Protocadherin-15 deficiency compromises sensory functions of lateral-line hair cells and retinal photoreceptor cells in *X. tropicalis*

We checked the deleterious effects of *pcdh15* knockdown on the hair cells of the neuromasts, the sensory organs of the lateral line (Seiler et al., 2005; Maeda et al., 2014). After the injection of MO e6-i6 into *X. tropicalis* embryos, we evaluated the activity of the MET channels of the neuromast hair cells in larvae. Because protocadherin-15 is a major component of the tip-links

that gate these channels (Kazmierczak et al., 2007; Maeda et al., 2014), we explored the permeability of the neuromasts to the vital dye FM1-43, a fluorescent, amphipathic styryl that rapidly accumulates in sensory hair cells after its entry via the MET channels (Gale et al., 2001). Live imaging in 2 and 3 dpf morphant larvae revealed a major loss of hair cells expressing functional MET channels, as assessed by a fourfold decrease of the FM1-43-stained area in individual cranial neuromasts as compared with mismatch MO-injected larvae ($120.6 \pm 15.5 \mu\text{m}^2$ [mean \pm SEM] in morphants [$n = 33$] versus $471.2 \pm 37.5 \mu\text{m}^2$ in age-matched controls [$n = 21$]; unpaired *t* test, $P < 0.0001$; Fig. 2 A, graph; and Fig. S2 A). Thus, *pcdh15* knockdown causes dysfunction of the MET channels in lateral line hair cells.

We then assessed retinal function in the morphant larvae by measuring electrotoretinogram (ERG) responses. These evoked potential responses in the retina are characterized by an initial negative deflection peak (the a-wave), followed by a positive peak (the b-wave), the amplitudes of which vary with the intensity of the light stimulation. In 4-dpf morphant larvae, the shapes and time to peak values of both the a- and b-waves were normal. However, the amplitudes of both ERG waves were smaller than those of the controls (Fig. 2 B).

We estimated the stimulus intensity at half-saturating amplitude ($I_{0.5}$) of these waves and their saturating amplitude

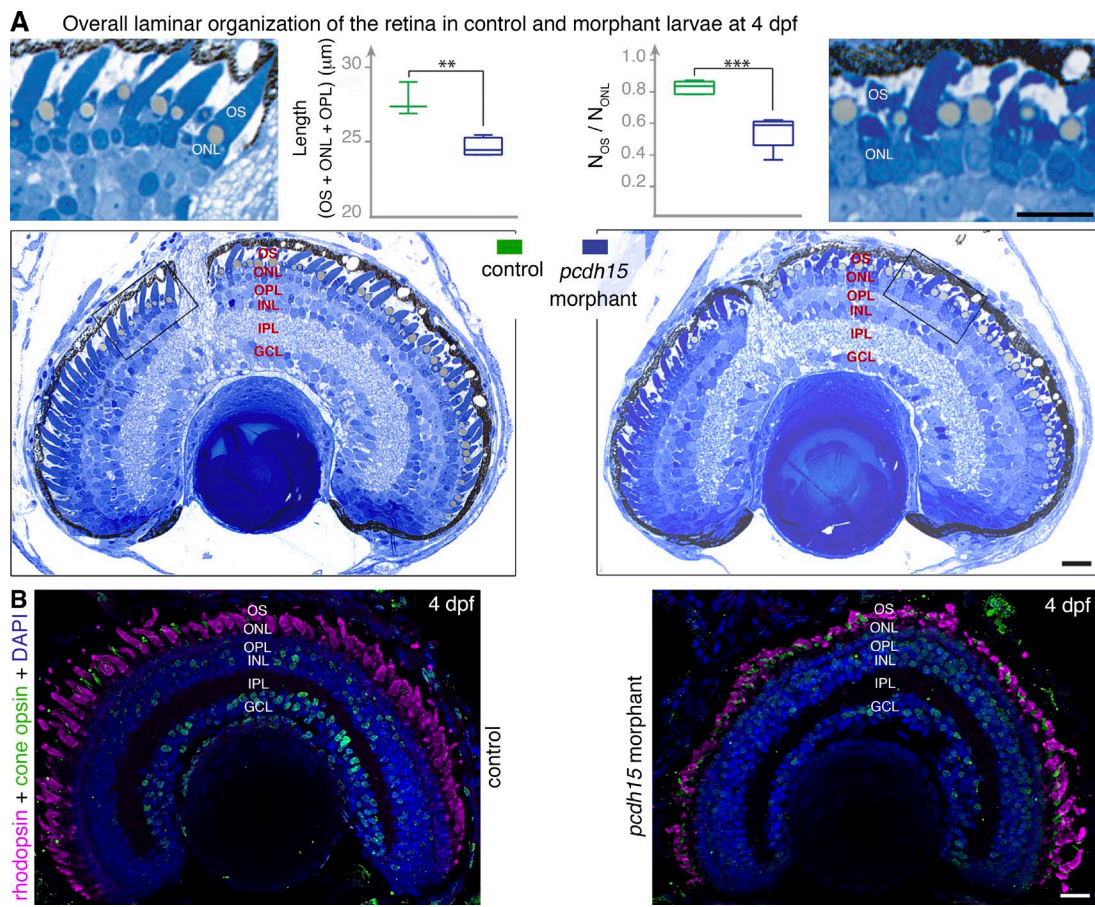


Figure 4. *Pcdh15* knockdown in *X. tropicalis* does not affect retinal morphogenesis. (A) Semithin sections of control and morphant retinas at 4 dpf. The retinal layer shows similar organization in morphants and control retina. However, a loss of alignment and shape alterations of the photoreceptor outer segments (OS) are seen in the morphants (see high magnification of the boxed areas). The outer retina is significantly thinner in the morphants: thickness of the OS, outer nuclear layer (ONL), and outer plexiform layer (OPL) ($L_{OS + ONL + OPL} = 24.6 \pm 0.3 \mu\text{m}$, mean \pm SEM, in morphants versus $27.7 \pm 0.6 \mu\text{m}$ in controls, $n = 3$ –4; unpaired t test, ***, $P = 0.005$). The ratio of the number of OS profiles (N_{OS}) to that of nuclei (N_{ONL}) is also significantly lower in morphants (0.55 ± 0.05 , mean \pm SEM, in morphants versus 0.83 ± 0.02 in controls, $n = 5$; unpaired t test, ****, $P = 0.0005$). (B) Cryosections of 4 dpf retinas stained with antibodies against rhodopsin (magenta) and cone opsin (green) show no evidence of opsin mislocalization in the morphant retina, but the shape and organization of both cones and rods are altered. INL, inner nuclear layer; IPL, inner plexiform layer; GCL, ganglion cell layer. Bars, 20 μm .

Downloaded from on June 2, 2017

(V_{max}) by fitting the Naka–Rushton equation $V/V_{max} = I^n/(I^n + I_{0.5}^n)$ to the ERG data (see Materials and methods). Values of $I_{0.5}$ were similar for control and morphant retinas (a-wave $I_{0.5}$, 12.68 ± 0.22 and 12.58 ± 0.15 ; b-wave $I_{0.5}$, 12.53 ± 0.22 and 12.72 ± 0.14 ; values reported as log₁₀[intensity in photons/ μm^2]). However, V_{max} was reduced in morphants by 40 and 30% for both a- and b-waves, respectively (F test: $P < 0.0001$ for both a- and b-waves; $n = 7$ controls, 13 morphants; Fig. 2 B). The smaller amplitude of ERG responses (V_{max}), with no change in sensitivity ($I_{0.5}$), suggests that the morphant larvae have a decreased number of functional photoreceptor cells.

Protocadherin-15 forms links connecting the calyceal processes and the outer segments of photoreceptor cells

We then investigated the distribution of protocadherin-15 in the photoreceptor cells of *X. tropicalis* larvae. We used an antibody recognizing the extracellular region of the human protocadherin-15 (the HPEX antibody) and a newly generated antibody directed against the juxtamembrane cytoplasmic region of *X. tropicalis* protocadherin-15 common to the two isoforms expressed (the XPJM antibody). Strong protocadherin-15

HPEX immunostaining was observed around the base of the photoreceptor outer segments in *X. tropicalis* larvae (Fig. S1 D). This staining corresponded to the calyceal processes stained for F-actin in 4 dpf larvae (Fig. 3 A). Immunogold labeling of permeabilized retinas with the XPJM antibody showed gold particles within the calyceal processes, both on the side of the outer segment and on the opposite side (Fig. S2 B). On non-permeabilized retinas immunolabeled with HPEX antibodies, we detected silver-enhanced nanogold particles all around the outside of the calyceal processes (Fig. 3 B and Fig. S2 C). When the immunostaining conditions were adjusted to maximize tissue preservation (see Materials and methods), we found that protocadherin-15 HPEX immunogold labeling was associated with links coupling the calyceal processes and the outer segment in the rods and cones (Fig. 3 C).

Abnormal outgrowth of rod basal disks and abnormal stacking of cone lamellae in *pcdh15* and *cdh23* morphant larvae

At 4 dpf, the *pcdh15* morphants displayed no gross defects of the organization of the retinal layers and no apoptotic or pyknotic nuclei indicative of cell degeneration in any of the cell

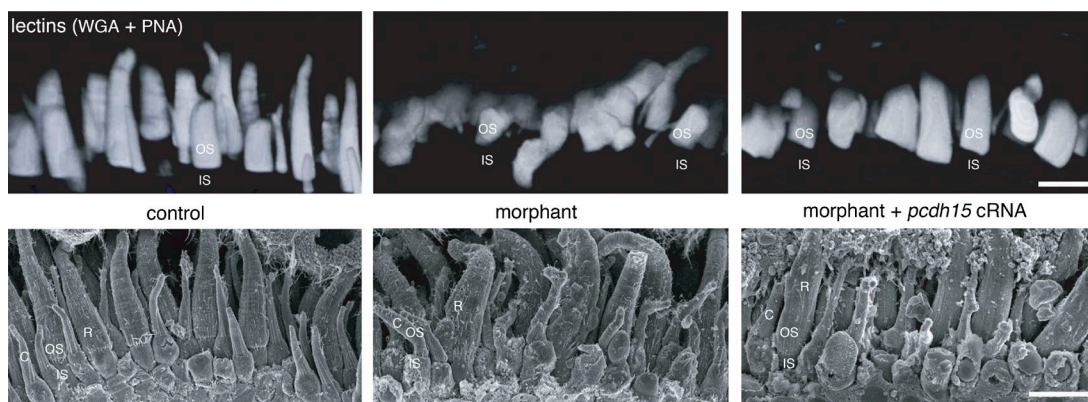


Figure 5. The photoreceptor outer segments are misaligned in *pcdh15* morphant larvae. 3D rendering of the confocal stacks obtained from acrylamide-embedded vibratome sections (150 µm thick) stained with fluorescent lectin (top) and from SEM micrographs (bottom), highlighting the orderly arrangement of the subretinal space in 4 dpf control retinas (left). In contrast, age-matched morphant retinas contain photoreceptors with missshapen, curved, and misaligned outer segments (OS; middle). The coinjection into the embryo of cRNAs encoding the protocadherin-15 CD1 and CD3 isoforms with the splice-blocking morpholinos essentially preserved the well-ordered organization and parallel alignment of the OS in the larva (right). IS, inner segment; C, cone; R, rod. Bars, 10 µm.

layers (Fig. 4, A and B). We detected a slight, but significant thinning of the photoreceptor cell layer in morphants (24.6 ± 0.3 µm [mean ± SEM], $n = 5$) as compared with controls (27.7 ± 0.6 µm, $n = 5$; unpaired *t* test, $P = 0.005$; Fig. 4 A). A thinning of the photoreceptor cell layer was also detected in the *cdh23* morphants (Fig. S3 B), suggesting that the loss of cadherin-23 also alters the architecture of photoreceptor cells. Photoreceptor cells in *pcdh15* (MO e6-i6, Fig. 4, A and B [right]; and Fig. S5 B; and MO e11-i11, Fig. S3 A) and *cdh23* (MO ATG, Fig. S3 B; and MO e9-i9, Fig. S3 C) morphant larvae lacked the uniform shape and parallel arrangement of the outer segments observed in control retinas, in which the inner and outer segments of adjacent photoreceptors are organized in a radial array oriented toward the pupillary opening (Eckmiller, 2004). A 3D reconstruction of the outer segments stained by lectin in MO e6-i6 morphant and control retinas showed that they were tilted in the morphants, providing further evidence of the abnormal alignment of adjacent photoreceptors (Fig. 5). This disorganization of the outer segment in morphant larvae was not observed if the full-length *pcdh15* cRNA was injected together with MO e6-i6 (Fig. 5), demonstrating the key role of protocadherin-15 in the morphogenesis of the photoreceptor outer segments.

We then analyzed the ultrastructure of the inner and outer segments of the photoreceptors by scanning and transmission electron microscopy (TEM). In 3 dpf control larvae, the developing rods had short, well-formed outer segments, whose bases were congruent with the apical surface of the inner segment. In contrast, in the 3 dpf morphant larvae, numerous rod outer segments had enlarged basal regions, with bulges protruding from the periphery of the outer segment (see Fig. S5 A). Quantification of scanning electron microscopy images showed that ~19% of rods in the 4-dpf MO e6-i6 morphants displayed abnormal bulges (Fig. 6 A and not depicted). Similar abnormalities of the rod outer segment base were observed in 4 dpf *cdh23* morphants (Fig. S3 C). We measured the basal diameter of lectin- or rhodopsin-stained rod outer segments and found that the mean values were significantly larger in morphants versus controls (Fig. 6 B; unpaired *t* test, $P < 0.001$). About 15.4% of rods in MO e6-i6 morphants and 10% in MO e11-i11 morphants had a diameter larger than two SDs greater than that of

the control mean, whereas <5% of the controls had a diameter greater than that threshold (Fig. 6 B and Fig. S1 E).

TEM analysis on 4 dpf *pcdh15* morphants showed that the rod outer disks were tightly packed and that the newly generated membranous stacks at the very base of the outer segment were well formed (Fig. 7, A and B). However, just above the edge of the inner segment, the new disks extended well beyond that edge, forming aberrant disk outgrowths corresponding to the bulges observed by scanning electron microscopy (Fig. 6 A and Fig. 7 B). We also observed changes of the cone outer segment shape in the morphants, which displayed a marked alteration of the distribution of taper angle (Fig. 6 C). We estimated that 74.2% of morphant cone outer segments exhibited an angle value exceeding that of the control mean by more than two SDs (Kolmogorov-Smirnov [K-S] test, $P < 0.0001$; Fig. 6 C). Outer-segment tilt was also markedly more variable in morphants versus controls (K-S test, $P < 0.0001$); we estimated that 64.8% of morphant cone outer segments exhibited a tilt angle greater than two SDs from the control mean (Fig. 6 C). TEM analysis of cone photoreceptors showed that the lamellae were well formed and tightly packed, with normal basal evaginations. However, unlike that of control larvae, the lamellae in the morphants were not flat but curved, and they had heterogeneous dimensions, with an abnormal base-to-apex decrease of surface area (Fig. S5 C).

Calyceal processes and their roots are absent from the cones of *pcdh15* morphant larvae, and their F-actin cytoskeleton is altered in rods

We then investigated whether *pcdh15* knockdown modified the calyceal processes of the rods and cones. In both humans and frogs, the calyceal processes of rod photoreceptors are embedded in incisures, axial indentations running the entire length of the outer segment (Eckmiller, 2000; Boesze-Battaglia and Goldberg, 2002; Sahly et al., 2012). Transverse TEM sections through the rod outer segments of 4dpf morphant larvae showed that the multilobular structure formed by the axial indentations was preserved (Fig. 7, A and B). The calyceal processes were still visible along the incisures in morphant rod outer segments (Fig. 6 D), except at the region of disk outgrowth, present in some rods (Fig. 6 A, asterisks; and

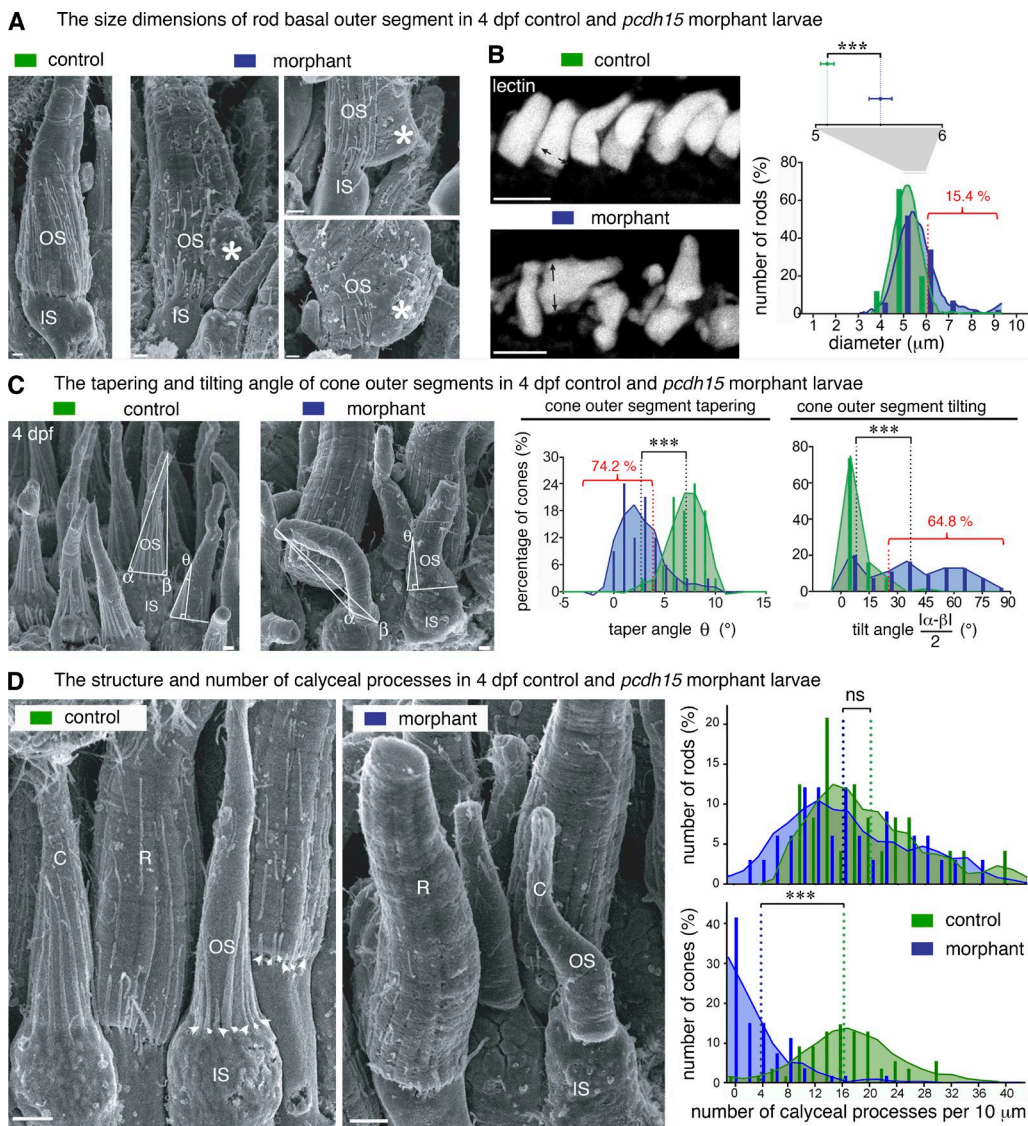


Figure 6. *Pcdh15* knockdown in *X. tropicalis* causes distinct morphological alterations to the rod and cone outer segments and the associated calyceal processes [scanning electron microscopy analyses]. (A) In scanning electron micrographs, rod outer segments (OS) of 4-dpf morphants often display basal swelling and bulges, observed in 24 of 126 (19%) of morphant rods ($n = 3$ retinas, 95% CI, 17.3–19.3%). Occasionally, the base of the OS (asterisks) extended well beyond the edge of the inner segment (IS). Calyceal processes (CPs) are not detected adjacent to the basal outgrowths (asterisks). (B) In control retinas (top left), the basal diameters of the rod OS stained with WGA lectin (white) have a distribution close to normal (green bar graph and curve), centered on $5.1 \pm 0.05 \mu\text{m}$ (mean \pm SEM, $n = 99$; D'Agostino-Pearson test, $P = 0.8$; skewness: 0.15). In morphant retinas, the diameters have a non-normal distribution (blue bar graph and curve), centered on $5.5 \pm 0.1 \mu\text{m}$ with a large positive skew ($n = 104$; D'Agostino-Pearson test, $P < 0.0001$, greater than two SDs from the control mean in 16 of 104 (15.4%) morphant rods. (C) At 4 dpf, control cone photoreceptors possess a slender OS coaxial with the IS and are characterized by a pronounced conical taper; both features are altered in the morphant cones. The OS tilt and taper were estimated on scanning electron micrographs by measuring the basal angles α and β and the taper angle θ at 5 μm from the IS-OS interface. The frequency histograms for tilt and taper angles show a narrow distribution of tilt angles centered on 5.8° (median value, $n = 68$) in control larvae, whereas in the morphants, the distribution is wider and flatter (median value, 36.5° ; $n = 54$), reflecting considerable variability in tilt (K-S test, ***, $P < 0.0001$; bin width, 10°); 35 of 54 (64.8%) of the morphant cone OS had a tilt more than 2 SD greater than the control mean. The taper angle of the morphant cone OS was significantly smaller than that of the controls ($2.7 \pm 0.4^\circ$, $n = 31$; and $7.1 \pm 0.3^\circ$, $n = 32$, respectively [mean \pm SEM]; bin, 3° ; K-S test, ***, $P < 0.0001$); 23 of 31 (74.2%) of morphant cone OS had a taper more than 2 SD less than the control mean. (D) We determined the number of calyceal processes (CPs) by counting them at their point of emergence (arrowheads) and plotted that number as linear density (number of CPs per 10 μm of IS-OS interface) for both rod (R) and cone (C) photoreceptors. Frequency distributions (bin width, 2 CPs per 10 μm) are significantly lower in morphant cones, but not in the rods. Mean densities in rods (in CPs per 10 μm): controls, 19.4 ± 1.6 (mean \pm SEM, $n = 24$); morphants, 16.5 ± 1.5 ($n = 33$); K-S test, $P = 0.27$. Mean densities in cones: controls, 16.7 ± 0.8 ($n = 53$); morphants 3.7 ± 0.6 ($n = 53$); $P < 0.0001$. Bars: (A and C) 1 μm ; (B) 10 μm ; (D) 5 μm .

Fig. 7 B). These calyceal processes were, however, more fragmented than they were in age-matched control rods (Fig. 6 A, asterisks; and Fig. 7 B). In contrast to rod outer segments, the cone outer segments in *X. tropicalis* have no incisures. The conspicuous ring of calyceal processes seen around the cone

outer segment in 4 dpf control larvae (Fig. 6 D, arrowheads) had almost disappeared in the morphant larvae; the distributions of the density of calyceal processes thus differed considerably between the morphants and the control (K-S test, $P < 0.0001$; Fig. 6 D, right). We counted 3.7 ± 0.6 calyceal pro-

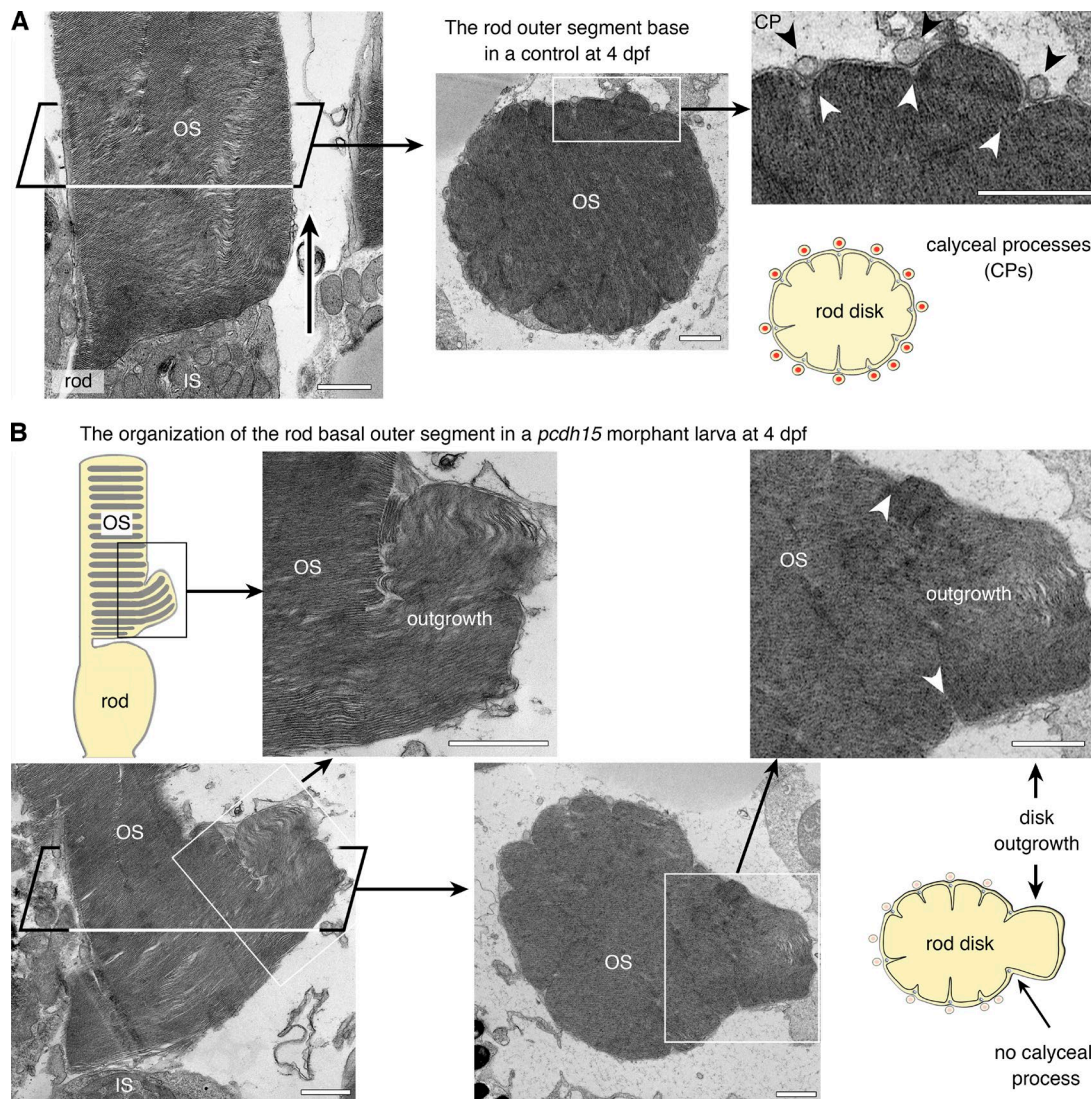


Figure 7. *Pcdh15* knockdown in *X. tropicalis* causes distinct morphological alterations to the rod and cone outer segments and the associated calyceal processes (TEM analyses). (A) In longitudinal (left) and transverse (right) thin sections, control rod photoreceptors have the expected shape, with cylindrical, multilobed outer segments (OS). The calyceal processes (CPs) can be seen all around the OS, lying within [black arrowheads] and occasionally between incisures demarcating the lobes of the rod disks (see diagram). The base of the OS is congruent with the tip of the inner segment (IS; left, arrow). (B) In morphant larvae, several rods display an enlarged base (boxed areas), which TEM analysis revealed to consist of packets of outgrown disks extending well beyond the IS-OS interface and folding laterally. These outgrown disks are confined within the boundaries of the delimiting incisures (white arrowheads). The CPs are visible adjacent to the unaffected region but not adjacent to the basal enlargements of the OS (middle and right). Bars, 1 μ m.

cesses every 10 μ m in cones in the morphants (mean \pm SEM, $n = 53$) versus 16 ± 0.9 ($n = 53$) in the controls.

The F-actin cytoskeleton of the calyceal processes is absent from the cones and altered in rods of *pcdh15* morphant larvae
 Immunofluorescence analyses in the morphant larvae showed preserved immunostaining patterns for rhodopsin and cone opsin in the outer segment, acetylated tubulin in the outer segment axoneme, the USH2 protein Adgrv1 around the base of the connecting cilium (Fig. 8 A), and peripherin/RDS, an integral membrane protein involved in disk formation and maintenance (Goldberg, 2006; Stuck et al., 2016), at the rim region of the rod and cone outer segments (Fig. S4 A). Immunostaining for the other USH1 proteins was too weak to assess any abnormality in the localization of those proteins in morphant photoreceptors (see Materials and methods). We then analyzed two populations of actin fila-

ments at the junction between the inner and outer segments of the photoreceptor cells: the longitudinal F-actin bundles forming the cores of the calyceal processes, including their roots, and the horizontal, subcortical F-actin network that extends from the connecting cilium toward the cell membrane, in the apical region of the inner segment (Fig. 8 B, middle). In the morphant rod and cone photoreceptors, staining for the transverse, subcortical F-actin network was observed close to the connecting cilium, although it extended over a smaller surface area than it did in the control photoreceptors (Fig. 8 C). In contrast, hardly any F-actin staining was detectable at the positions of the calyceal processes, either in the roots located in the inner segments of both rods and cones or along the outer segments (Fig. 8 B). Immunostaining for espin, an F-actin cross-linking protein present in the calyceal processes (Sahly et al., 2012), was also much weaker in the morphant photoreceptors (Fig. S4 B). We quantified the F-actin staining in 4 dpf photoreceptors by the ratio of F-actin fluorescence intensity

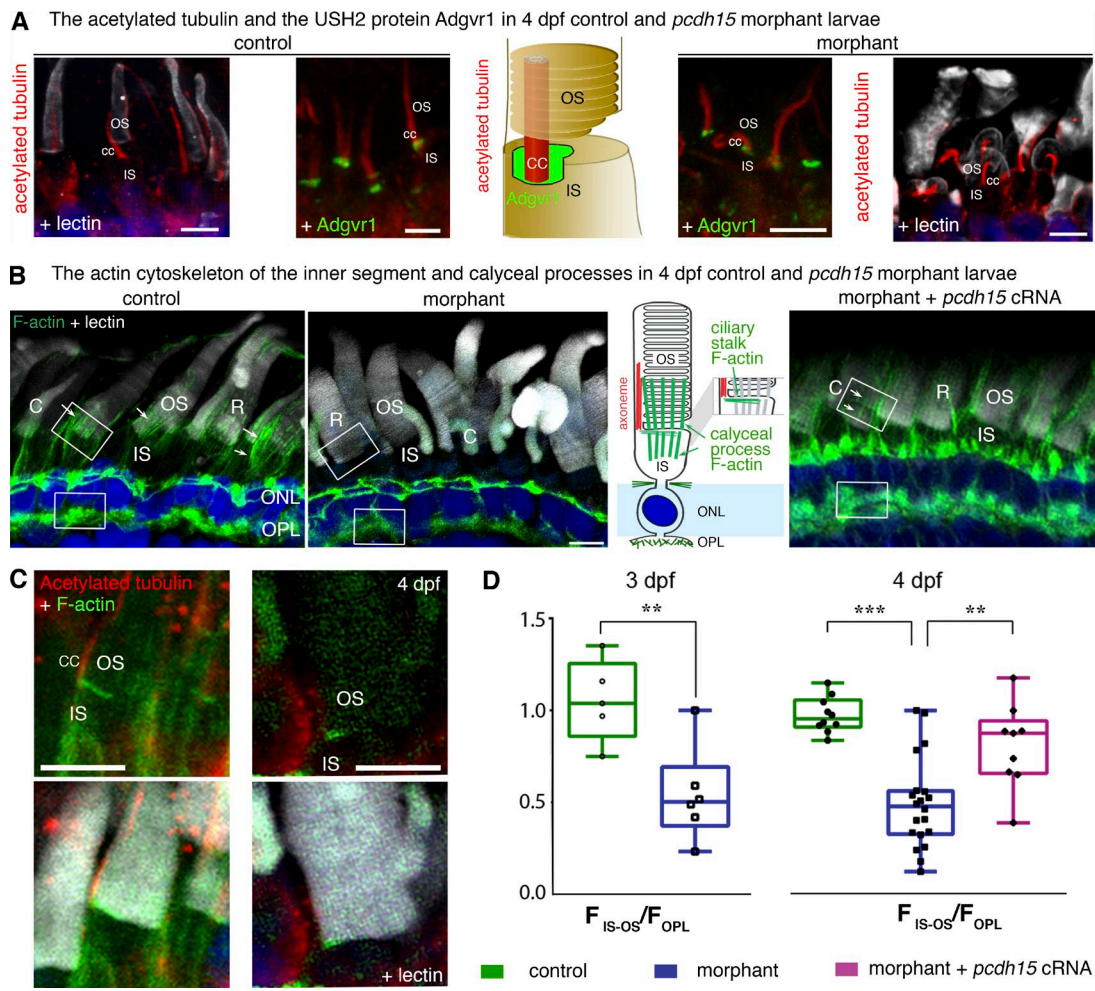


Figure 8. The actin cytoskeleton of the calyceal processes and their roots is disrupted in *pcdh15* morphant larvae. (A) The axoneme, stained with antibodies against acetylated tubulin (red), is present in the morphant cone photoreceptors, but it is often curved and bent. The typical distribution of the USH2 protein Adgvr1 (green) at the base of the axoneme, in the periciliary ridge complex, is preserved in morphant photoreceptors. (B) At the inner segment (IS)-outer segment (OS) interface, there are two F-actin networks: the transverse F-actin network at the apical surface of the IS, and the longitudinal F-actin bundles of the calyceal processes and their roots (arrows). In 4-dpf morphant retinas, morphants display less phalloidin staining at the IS-OS interface (middle) than do the age-matched controls (left). F-actin staining in morphant photoreceptors is restored by the coinjection into the embryo of *pcdh15* cRNAs with the *pcdh15* MO e6-i6 (see arrows in the right panel). (C) The transverse F-actin network (green) can still be observed in a morphant photoreceptor. (D) Measurements of F-actin fluorescence intensity in the IS-OS interface (F_{IS-OS}) compared with the subjacent region of the outer plexiform layer (OPL) (F_{OPL} , taken as a reference) showed an F_{IS-OS}/F_{OPL} ratio that is 50% lower in the morphants than in the controls. The F-actin cytoskeleton was partially preserved in the retinas of 4-dpf morphants after the coinjection into the embryo of *pcdh15* cRNAs and *pcdh15* MO e6-i6 (F_{IS-OS}/F_{OPL} ratio 20% smaller than in controls). The F_{IS-OS}/F_{OPL} ratio at 3 dpf: controls, 1.05 ± 0.10 ($n = 5$); morphants, 0.54 ± 0.1 ($n = 6$), mean \pm SEM; unpaired *t* test, **, $P = 0.007$. At 4 dpf: controls, 0.97 ± 0.03 ($n = 10$); morphants, 0.48 ± 0.06 ($n = 20$); morphants + cRNAs, 0.81 ± 0.08 ($n = 9$); unpaired *t* tests: controls versus morphants, ***, $P < 0.0001$; morphants versus morphants + cRNAs, **, $P = 0.002$; controls versus morphants + cRNAs, $P = 0.05$. Bars, 5 μ m.

in the region of the calyceal processes to that in the synaptic region of the same photoreceptor. That ratio was 50% lower, on average, in morphants than in controls (unpaired *t* test, $P < 0.0001$; Fig. 8 D). Notably, the reduction of F-actin staining was only of 20% ($P = 0.05$) in the calyceal processes and their roots when the full-length *pcdh15* cRNA was coinjected into *X. tropicalis* embryos with MO e6-i6 (Fig. 8, B and D, right). Protocadherin-15 is thus required for the normal development and/or maintenance of the calyceal processes of both rods and cones.

Discussion

Our results show that the development and maintenance of the calyceal processes in cone and rod photoreceptor cells are

critically dependent on protocadherin-15, the protein defective in the USH1F genetic form of USH1. The results show these processes are required for the normal growth and to shape the photoreceptor outer segment. The results identify defects in the calyceal processes as new mechanisms underlying the retinal pathogenesis observed in USH1.

The localization of protocadherin-15 in *X. tropicalis* photoreceptors is consistent with its involvement in the links connecting the calyceal processes to either the outer segment in rods and cones or to other calyceal processes in cones. We have previously shown, in frog and macaque photoreceptors, that cadherin-23 is also present in those outer-segment regions (Sahly et al., 2012). Based on the tip-link composition (Söllner et al., 2004; Michel et al., 2005; Kazmierczak et al., 2007; Goodyear et al., 2010; Sotomayor et al., 2012), we propose

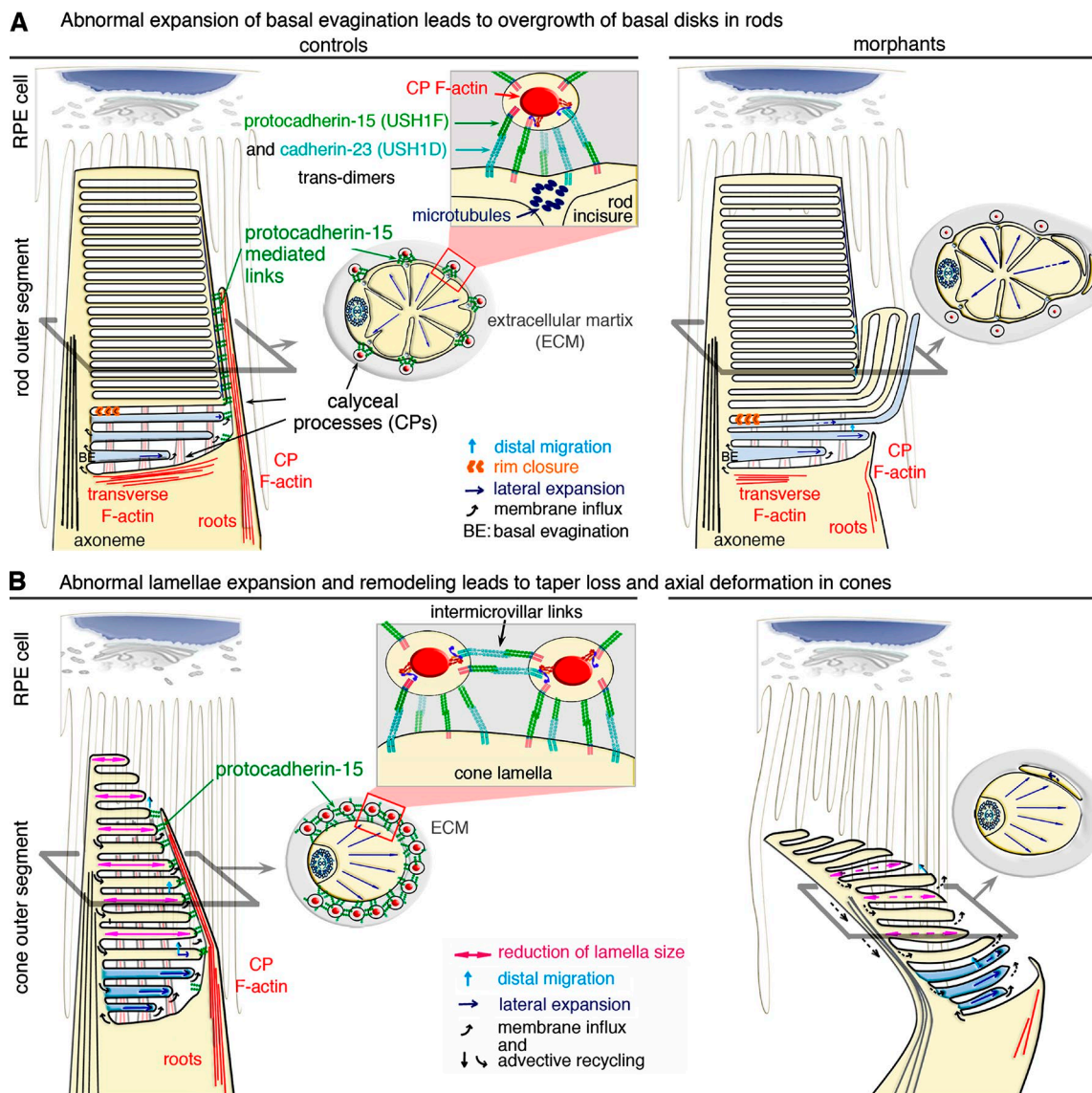


Figure 9. Model of the structural defects observed in the photoreceptors of morphant larvae. (A and B) In rod (A) and cone (B) photoreceptor cells, the basal evaginations (BEs) are formed with their leading edge exposed to the extracellular space. Calyceal processes (CPs) filled by F-actin (red) surround the base of the outer segment (OS) in control rods and cones (A and B, left). Links formed by trans-interactions between protocadherin-15 and cadherin-23 likely couple CPs to the OS membrane and to other CPs in the cones. The formation of trans-homotypic links, made up of either protocadherin-15 (Indzhykulian et al., 2013) or cadherin-23 cannot be excluded (A and B). (A, top left) Rod BEs form a continuous membrane system, topologically equivalent to cone lamellae. Lateral expansion of the BEs is tightly coupled to disk formation and distal displacement. Rim closure creates a discontinuity between the disk and the plasma membrane, precluding membrane redistribution in the plasmalemma. (top right) Uncontrolled lateral expansion of the nascent disks might lead to aberrant outgrowths, as shown in the *pcdh15* morphant rods. In the morphant rods, the internal cytoskeleton of microtubules along the incisures may sustain the persisting CPs, although the F-actin cytoskeleton within the processes is markedly decreased. (B) Unlike rods, cones have no incisures, and the CPs do not anchor to microtubules. (bottom left) Preservation of the cone OS shape requires a balanced distribution of forces and flows. Membrane input into the membrane folds of the cone lamellae at the OS base is equilibrated by advective recycling in the plasmalemma and apical shedding of older lamellae. This results in the lateral expansion, distal displacement, and progressive resizing of lamellae by retinal pigment epithelium (RPE) cells. (bottom right) In *pcdh15* morphant cones lack CPs; disturbance of the balance between these antagonistic forces causes taper loss and an abnormal axial curvature of the OS.

that the outer segment and calyceal process photoreceptor links (~180 nm long) are formed by trans-interactions between anti-parallel protocadherin-15 and cadherin-23 heterodimers (see Fig. 9 A). Similar cadherin-composed links have been described in the intestinal epithelium, where they play a key role in the elongation and maintenance of actin-based protrusions of enterocytes. Protocadherin-24 and mucin-like protocadherin form trans-heterotypic links that bridge adjacent intestinal microvilli. The knockdown of *pcdh24* in Caco2 cells (epithelial colorectal

adenocarcinoma cells) has been shown to impair the formation of links between microvilli, resulting in a shortening of the microvilli because of F-actin disassembly (Crawley et al., 2014). A similar mechanism may account for the loss of calyceal processes in *pcdh15* morphants, which is supported by the marked decrease of F-actin cytoskeleton that compose these processes and their roots (Fig. 8 D). The five main USH1—myosin VIIa, harmonin, cadherin-23, protocadherin-15, and sans—have been involved at the core of the hair-cell MET machinery, with myo-

sin VIIa, harmonin, and sans anchoring the cadherin-composed tip-link to the actin filaments in the stereocilia (Richardson et al., 2011). A similar protein complex involving myosin VIIB, harmonin, and ANKS4B, a paralog of sans, is required to anchor the cadherin-mediated, enterocyte intermicrovillus links to the microvilli actin cores (Crawley et al., 2014, 2016). Because the five main USH1 proteins are also located at the calyceal processes of frog and primate photoreceptors (Sahly et al., 2012), the cadherin-mediated links of the calyceal processes are probably anchored to their actin cytoskeleton, most likely through their interaction with myosin VIIa, sans, and harmonin (Fig. 9).

According to the prevailing model of outer-segment biogenesis, new disks/lamellae in rods and cones form from the emergence of basal-membrane evaginations around the connecting cilium (Steinberg et al., 1980). Our findings suggest that the first steps in outer-segment biogenesis are independent of *pcdh15* and *cdh23*. In the morphant photoreceptors, the development of disks/lamellae was initiated correctly at the base of the outer segment. The successive, basal evaginations extended from the connecting cilium toward the opposite edge of the inner segment (Fig. 9, A and B), similar to that observed in wild-type mice (Steinberg et al., 1980; Volland et al., 2015). In contrast, membrane abnormalities were observed in both rods and cones after that initial step. In rods, the membrane abnormalities included the giant “bulges” formed by abnormally expanding membrane folds (Fig. 9 A), and in cones, the abnormalities included the heterogeneous dimensions of the lamellae, which caused abnormal tapering and tilting of the outer segment (Fig. 9 B). The F-actin cytoskeleton, which forms the core of the calyceal processes and their roots, was significantly decreased in both the rods and cones of *pcdh15* morphant larvae. Thus, the F-actin–filled ring structure, normally formed by the calyceal processes and their associated links around the outer segment, emerges as a key element regulating the size of mature disks/lamellae.

How do defects in the calyceal processes cause the observed outer-segment abnormalities? A key feature of the outer segments of the photoreceptors is their daily renewal. The rod outer segments are entirely replaced over the course of 1–6 wk in most vertebrates, including mice and frogs (Young, 1967), and the frequency of membrane shedding at the tip of the cone outer segment suggests similar rates of cone renewal (Eckmiller, 1997). In rods, when the evaginations reach the diameter of the inner segment, the nascent disks become separated from the outer-segment plasma membrane and from the other disks. In cones, the outer-segment plasma membrane remains continuous, and the lamellae simply emerge from the basal evaginations (Fig. 9, A and B). The mature, phototransductive disks/lamellae then gradually move upward until they reach the distal tip of the outer segment, where they are shed and subjected to phagocytosis by the surrounding retinal pigment epithelium (RPE) cells (Young, 1967; Steinberg et al., 1980).

Different types of force likely develop in the outer-segment membrane during the formation and displacement of the newly formed disks/lamellae. The calyceal processes should, therefore, experience continuous, mechanical constraints along their entire length. It has been suggested that actin-based myosin motors pull the basal evaginations at their rims, gradually expanding them to the diameter of the inner segment (Dosé et al., 2003; Corless, 2012). Actin protrusion forces that develop according to such a mechanism could range from a few tens to a few hundreds of piconewtons (Marcy et al., 2004). Similar

myosin-driven forces could act beyond the basal evaginations at the sites of contact between the newly formed disks/lamellae and the calyceal processes, as suggested by the overgrowth of the disks observed when the calyceal processes are missing. Moreover, passive forces must develop in the outer-segment membrane because of the elastic energy stored within it, particularly in the cones, because of the continuity of the lamellae. Two such forces are the tension force, associated with the stretching energy of the membrane, and the torque force, associated with its bending energy. Because of the very high area-to-volume ratio of the disks/lamellae, the outer-segment stability probably requires that membrane-stretching energy be kept very low. However, the tendency of the membrane to minimize its bending energy should result in a net inward force communicated to the calyceal processes at the rims of the lamellae on the order of a few tens to ~100 pN/fold. Indeed, for a typical lamella, that force can be estimated as $F \approx (\pi^2\kappa)/\rho \sim 94$ pN, assuming a radius of $R = 5$ μm , a folding curvature radius or $\rho = 9$ nm (Corless, 2012), and a membrane bending modulus of $\kappa = 0.005 k_B T$.

Whatever the origins of the forces (active or passive) developing in the membrane of the outer segment, they must be properly controlled to prevent the outgrowth of the disks/lamellae and their movement relative to each other. Based on the typical forces that a single tip-link are thought to sustain (~10 pN for its resting tension and at least ~30 pN during sound stimulation; Jaramillo and Hudspeth, 1993; Gillespie and Cyr, 2004; Prost et al., 2007), the ring formed around the outer segment by the calyceal processes could accommodate forces ranging from a few hundred piconewtons to a few nanonewtons. In both cones and rods, the calyceal processes could, therefore, easily withstand the protrusive forces of the growing basal evaginations. Our results suggest that the calyceal processes of cones are also involved in maintaining the tapering profile of the outer segment beyond its basal region. In that respect, such structural irregularities or bending of the cone outer segments might be detected in patients by using directional reflectance measurements (Miloudi et al., 2015). In rods, an internal cytoskeleton of microtubules is present along the incisures providing an additional cytoskeleton coupling the outer segment to the calyceal processes; its persistence in *pcdh15* morphant rods may explain why the disks remain aligned above the outer-segment basal region (Fig. 9 A). The recent finding that marshalin, a microtubule binding protein, interacts with the cytoplasmic region of cadherin-23 suggests a possible mechanism for anchoring cadherin-23–composed links to the microtubules of the outer segment (Takahashi et al., 2016). Other structures might contribute to the normal alignments of the outer-segment disks/lamellae. Notably, the long, actin-based microvilli, extending from the apical surface of the RPE cells, which envelop the outer segments of both rods and cones at their apex, and, remarkably, surround the entire outer segment, down to the inner segment in mouse photoreceptors (Bibb and Young, 1974; Bonilha et al., 1999; Nawrot et al., 2004), may also provide mechanical support to the outer-segment morphogenesis and have a more critical role in species lacking well-developed calyceal processes (Fig. 9, A and B).

Finally, the oversized, rod basal disks appear before the curved cones with lamellae of abnormal size in *X. tropicalis* morphants, reproducing the chronological sequence observed in patients with USH1. Indeed, USH1 retinopathy is classified as a rod–cone dystrophy, with the initial appearance of rod abnormalities, which rapidly worsen, followed by progressive

cone dysfunction and photoreceptor cell degeneration (Flores-Guevara et al., 2009; Malm et al., 2011a,b). Overall, our results reveal the existence of a new retinal pathogenic process, which we propose to name calyceopathy.

Materials and methods

Ethics statement

Animal care, handling, and experimentation conformed to institutional guidelines and were covered by institutional license C 91-471-102. Protocols were approved by the “Comité d’éthique en experimentation animale 59” and procedure 42 and were authorized by the “Ministère de l’Education Nationale, de l’Enseignement Supérieur et de la Recherche” under the reference APFIS998.

Embryos and microinjection

X. tropicalis embryos were obtained by in vitro fertilization, according to conventional procedures and were staged as described by (Nieuwkoop and Faber, 1967); 2, 3, and 4 dpf correspond to stages 28–33, 35–40, and 42–44, respectively. Photoreceptors can be discerned in the *Xenopus* retina as early as Nieuwkoop-Faber stage 33 (Hollyfield and Witkovsky, 1974; Stiemke et al., 1994). At stage 40, rods are morphologically distinct from cones, and at stages 44–46, the rod outer segments acquire the mature cylindrical form and their inner segments lose the oil droplet, which is retained by the cones (Chang and Harris, 1998); at stage 44, *Xenopus* tadpoles possess a functional visual system (Dong et al., 2009). Embryos were grown to the desired stage in modified Marc’s modified ringer (MMR) medium (100 mM NaCl, 2 mM KCl, 1 mM MgCl₂, 2 mM CaCl₂, and 5 mM Hepes, pH 7.5) used at a strength of 0.05× up to gastrulation and at 0.1× thereafter. Embryos were anesthetized with tricaine methanesulfonate (0.04% MS-222 in 0.1× MMR), other than for electrophysiological recordings (Wilson et al., 2009).

The design of antisense morpholino nucleotides (GeneTools) was based on the sequences of target sites obtained from the genomic DNA of the *X. tropicalis* strains used in the study.

In the following information, the sequences of the MOs used in the study are indicated in uppercase letters, followed by the corresponding controls, in which the mismatch nucleotides are indicated with lowercase letter. The underlined portions correspond, for the splice blockers, to the exon sequences on the corresponding pre-mRNA, and for the translation blockers, to the ATG codon on the corresponding mRNA.

Pcdh15 MO splice site blockers (the numbers indicate the targeted exon for e, and the flanking intron for i): *Pcdh15* i5-e6 acceptor: 5'-CTGCCTGTAATAGAAACAGTGGGTT-3', 5'-CTCCCTCTATTCAAACACTGGGTT-3'; *Pcdh15* e6-i6 donor: 5'-ATGATTAGAATATACCAACCAATGA-3', 5'-ATCATTACAATATAGAACGAATCA-3'; *Pcdh15* i10-e11 acceptor: 5'-GCGCCGTAAGCTGTAGATGAAA-3', 5'-GCCCTAAGCTCTACATCAAAAAA-3'; *Pcdh15* e11-i11 donor: 5'-TGATTGTTGGAAGCGGTACCTTCT-3', 5'-TGATTCTTCGAACCCTAGCTCT-3'. *Cdh23* MO splice site blockers: *Cdh23* e2-i2 donor: 5'-AAATTGCTTGCTCACCCCTGAGTT-3', 5'-AAATATCCCTCCTCACCGTCAGTT-3'; *Cdh23* e9-i9 donor: 5'-GAACATTTAGGACACCTACGATCT-3', 5'-GAAGAATTTACGACACGTACCATCT-3'; *Cdh23* translation-blocking morpholino (MO ATG): 5'-GAAATCTTGTTGCTCATAGTTC-3'; *Myo7a* translation-blocking morpholino (MO ATG): 5'-GGCGTGGTACATCCTCACCACTC-3', 5'-GGCCTCGTAGATCCTGAGCACCCTC-3'; *Ush1g* translation-blocking morpholino (MO ATG): 5'-GTGATAGCGCCCGTCCATCTGCAT-3', 5'-GTCCATACCGGCCCTCCATCCTCCAT-3'; *Ush1c* translation-blocking morpholino (MO ATG): 5'-ACTCTCTGGCTATCTCCTCTCCAT-3', 5'-ACTCTGTGCGCTATGTTC-3'.

GTGTCCAT-3'; MO Standard control (targeting human β-globin transcripts): 5'-CCTCTTACCTCAGTTACAATTATA-3'.

All the injected MOs were conjugated with red fluorescent lisamine to facilitate analysis. Loss of function was achieved by microinjecting 2.5 pmol of antisense MO oligonucleotides in water (GeneTools) into one or two blastomeres of *X. tropicalis* at the one-cell or two-cell stage. Five nucleotide-mismatch and standard control (GeneTools) oligonucleotides were used as controls.

RT-PCR and in vitro transcription

Total RNA was extracted from dissected larval eyes (at 4 dpf) with the RNeasy kit (QIAGEN) and reverse-transcribed with oligo(dT) primers and the Superscript II enzyme (Thermo Fisher Scientific). PCR was performed on the cDNA with the Phusion DNA polymerase (Thermo Fisher Scientific). Putative CD1 and CD3 cDNA sequences were identified by BLAST searches in Xenbase (*X. tropicalis* genome 8.0; James-Zorn et al., 2015) and were used to design specific oligonucleotides for the amplification and cloning of full-length cDNAs, which were then checked by Sanger sequencing. The sequences of the *pcdh15* CD1 (GenBank cession no. KX463408) and *pcdh15* CD3 (accession no. KX463409) cDNAs from *X. tropicalis* have been deposited in GenBank. Protein domain graphs were generated with DOG 1.0 software (Ren et al., 2009; Fig. 1 A).

The full-length *pcdh15* CD1 and CD3 cDNAs were inserted into the pCS2+ plasmid, in frame, with a sequence encoding the *Xenopus* chordin signal peptide (Larraín et al., 2001). The cDNAs were transcribed to generate cRNAs in vitro, with the Message Machine Sp6 transcription kit (Thermo Fisher Scientific), according to the manufacturer's instructions. We checked cRNA quality by electrophoresis in denaturing gels. For experiments requiring the coinjection of MOs and cRNAs, we microinjected ~500 pg of cRNA into *X. tropicalis* at the one-cell stage.

We evaluated the effects of MOs designed to interfere with splicing, by performing RT-PCR on cDNA derived from RNA extracted from whole animals or from dissected, larval eyes (at 4 dpf). The abnormal RT-PCR products were sequenced, revealing exon skipping, intron retention, and the use of alternative splice sites. Nonsense-mediated mRNA decay was evaluated by semiquantitative PCR analysis, with ImageJ software (National Institutes of Health; Šindelka et al., 2006) analysis of the amplification products of GAPDH (*gapdh*, GenBank NM_001004949.2) or ornithine decarboxylase-1 (*odc*, NM_001005441.1) cDNA for normalization. The primers used were as follows: for *pcdh15* exon 6: forward 5'-CAAATCCTAATGAACGACGG-3' and reverse 5'-AGCACTGCTGTAGTTGGTTC-3'; for exon 11: forward 5'-GATAGCTTCAGACGGCACC-3' and reverse 5'-GCATAGCTTCAGTCAAGTCAAG-3'. For *cdh23* exon 9: forward 5'-TGACATTAATGATAATGCTCC-3' and reverse 5'-CAGAACAGTAGCACTGCTG-3'. For *gapdh* forward 5'-GCTCCTCTGCAAAGGTAT-3' and reverse 5'-GGGCCATCCACAGTCTCTG-3'. For *odc* 5'-GCCATCGTAAGACTCTCTCC-3' and reverse 5'-CATTGGGTGATTCTTGCCAC-3'.

Antibodies and other staining reagents

A rabbit antiserum was raised against a peptide corresponding to the constant intracellular region of *X. tropicalis* protocadherin-15 located between the transmembrane domain and the variable cytoplasmic domain (amino acids 1,400–1,444, accession no. Q96QU1; XPJM in Fig. 1 A). The antibody was affinity purified with the corresponding antigen coupled to an NHS-column (GE Healthcare). The following affinity-purified, commercial primary antibodies and reagents were used: sheep polyclonal anti-human protocadherin-15 antibody (AF6729; R&D Systems), raised against the entire extracellular portion of the protein (amino acids 27–1376, accession no. Q96QU1; HPEX in Fig. 1 A); mouse monoclonal anti-glutamylated tubulin (GT335; ALX-

804-885; Enzo Life Sciences); mouse anti-rhodopsin (MAB5316; EMD Millipore); goat polyclonal anti-cone opsin (sc-22117; Santa Cruz Biotechnology, Inc.); and mouse polyclonal anti-PRPH2 antibody (ab172264; Abcam). Phalloidin conjugated to Alexa Fluor 488 (A12379) or Alexa Fluor 594 (A12381; Molecular Probes) was used to label F-actin. An Alexa Fluor 680 conjugate of WGA (W32465) and an Alexa Fluor 647 conjugate of PNA (L32460; Molecular Probes) were used to stain the outer segments of rod and cone photoreceptors, respectively. DAPI (Sigma-Aldrich) was used to stain cell nuclei.

Tissue processing and imaging

Up to 4 dpf, *X. tropicalis* larvae (tadpoles) were killed in tricaine methanesulfonate and stored in RNALater for RNA extraction or immediately fixed in 4% PFA (in 100 mM sodium phosphate supplemented with 0.05 mM CaCl₂). Tadpoles were fixed by incubation overnight at 4°C in this fixative. They were then washed and stored in 0.1 M sodium phosphate until further processing.

Tadpoles destined for cryosectioning were infiltrated with 30% sucrose in PBS and then embedded in 7% pig gelatin (type A)/15% sucrose in PBS and rapidly frozen in isopentane cooled to -50°C. Gelatin blocks were stored at -80°C. We cut 10–20-μm-thick sections, perpendicular to the main axis of the embryo from these blocks in a Microm cryostat and mounted them on glass slides in Fluoromount-G (SouthernBiotech).

We obtained thick (150–200 μm) vibratome sections, by washing PFA-fixed tadpoles in 100 mM sodium phosphate, embedding them in 4% low-melting point agarose in 0.7× PBS, and cutting sections on a vibratome (speed 2, frequency 9; Leica Biosystems). Alternatively, tadpoles were infiltrated with 10% acrylamide/tetramethylmethylenediamine in PBS (Germroth et al., 1995) for 1 h at RT, transferred to fresh acrylamide, and polymerized with ammonium persulfate. The blocks were then cut on a Leica Biosystems vibratome, and sections were mounted on glass slides in Fluoromount-G (SouthernBiotech). Acrylamide stabilizes and preserves the relative positions and shapes of the outer segment during sectioning, making it possible to reconstruct large volumes containing multiple rows of lectin-stained photoreceptors.

Immunofluorescence analysis was performed on agarose and acrylamide vibratome sections and on cryosections (Moreau-Fauvarque et al., 2003). Samples were blocked by incubation in PBS, supplemented with 0.2% gelatin (Prolabo) and 0.25% Triton X-100, incubated overnight with the appropriate primary antibody and/or Alexa-labeled lectin at 4°C, rinsed in PBS, incubated with the appropriate secondary antibody for 1 h at RT, rinsed in PBS, and counterstained with DAPI. The secondary antibodies used were: Alexa Fluor 488-conjugated goat anti-rabbit IgG, Alexa Fluor 488-conjugated goat anti-mouse IgG, Alexa Fluor 594-conjugated goat anti-rabbit IgG, Alexa Fluor 594-conjugated goat anti-mouse IgG, Alexa Fluor 647-conjugated donkey anti-mouse IgG, and Alexa Fluor 488-conjugated donkey anti-sheep antibody, all from Invitrogen. Confocal imaging of cryo- and vibratome sections was performed at RT with an upright FV-1000 (Olympus), with the following wavelengths: 405 (diode), 440, 488 (Argon), 515 (Argon), 559 (diode), and 635 nm (diode), and with an inverted Olympus FV-1000 and the following wavelengths: 405 (diode), 440, 488 (Argon), 515 (Argon), 559 (diode), and 635 nm (diode). The following objectives were used: 20× oil (NA 0.85), 40× oil (NA 1.30), and 60× oil (NA 1.40). Images were converted into high-resolution .tiff format and processed with ImageJ (version 1.43). Confocal stacks were visualized three-dimensionally using the 3D Viewer plugin for ImageJ.

For embedding in plastic, whole tadpoles or agarose vibratome sections were postfixed by incubation for 2–3 h in 2.5% glutaraldehyde/100 mM sodium cacodylate, then incubated in 1% osmium tetroxide/100 mM sodium cacodylate, dehydrated in ethanol series, and infiltrated with EPON resin/araldite (Mollenhauer, 1964). Tadpoles

were then hemisected sagittally, flat-embedded in silicone molds, and cured (24 h at 60°C). A Leica Biosystems Ultracut was used to cut sections of the eye perpendicular to the main axis of the tadpole, in the plane of the optic nerve. For histologic analysis, semithin sections (500 nm) were mounted on glass slides, dried, and cover-slipped with a nonaqueous medium (Diamount; Diapath). Slides were then scanned with a NanoZoomer 2.0 high-throughput scanner equipped with a 3-charge-coupled device (CCD) time-delay integration camera (Hamamatsu Photonics). For ultrastructural analysis, thin sections (70–80 nm) were contrast-stained with modified Sato's lead (Hanaichi et al., 1986) and observed in a Tecnai T12 electron microscope (FEI) operating at 120 kV. Images were collected with side-mounted 2000 × 2000 Veleta (Olympus) and bottom-mounted Orius (SC1000, Gatan Inc.) CCD cameras, controlled with Digital Micrograph (Gatan Inc.) software, and subsequently processed with ImageJ.

Pre-embedding immunoelectron microscopy was performed on agarose vibratome sections. For immunolabeling with antibodies directed against extracellular epitopes, sections were incubated for 2 h at room temperature in a blocking solution containing 5% BSA and 0.1% cold-water fish skin gelatin (Aurion) in PBS, pH 7.4, washed twice in 0.2% acetylated BSA (BSA-c; Aurion) in PBS, and incubated for at least 24 h in the same solution supplemented with the primary antibody. The sections were washed, and the primary antibody was detected with protein A conjugated to 10 nm gold particles or nanogold-conjugated secondary antibodies. The sections were washed in antibody solution and PBS, then postfixed in glutaraldehyde, and prepared for embedding in plastic and ultrathin sectioning, as previously described (Furness and Hackney, 1985; Sahly et al., 2012).

For morphological analysis by scanning electron microscopy, agarose vibratome sections through the larval eye were postfixed in 2.5% glutaraldehyde and prepared according to the OTOTO protocol, as previously described (Sahly et al., 2012). Images were taken with an JSM6700F electron microscope operating at 5 kV (JEOL).

Brightness and contrast adjustments were made to images, and final composite images were generated with FigureJ plugin for ImageJ, and Photoshop CS3 (version 10.0; Adobe). Morphometric and other statistical analyses were performed with GraphPad Prism 6 software version 6.00 for Windows (GraphPad Software).

FM1-43 uptake experiments

For the selective labeling of neuromast hair cells, live tadpoles were exposed to 2.5 mM FM 1–43 (Thermo Fisher Scientific) in embryo medium for 30 s. The larvae were rinsed three times in medium and then anesthetized in MS-222. Fluorescent neuromasts were imaged with a confocal laser microscope or a spinning disk microscope. Live time-lapse imaging at 27°C was performed with a CSU-X1 spinning-disk scan head (Yokogawa Electric Corporation), mounted on a DM6000 upright microscope (Leica Biosystems), with 10 and 20 water-dipping objectives. Images were acquired using a CCD CoolSnap HQ2 (Roper Technologies) camera.

In the z-stacks obtained by live imaging, we measured the cross section of cranial neuromasts labeled with FM 1–43 (outlined in Fig. 2 A and Fig. S2 A), using ImageJ.

Electroretinography

ERG was performed on tadpoles at 4 and 5 dpf, with a NeuroNexus multielectrode linear array (Neural Probe, A1 × 16-3 mm-50-703) coupled to a white light-emitting diode (LED) (MWHL3; Thorlabs, Inc.). LED output was calibrated with a spectrometer (USB2000+; Ocean Optics), with OceanView software (Ocean Optics). Stimulation was performed at different light intensities, by varying LED output with a Thorlabs, Inc. LED controller (LEDD1B, T-Cube LED Driver;

Thorlabs, Inc.). All the recordings were made in a Faraday cage. Tadpoles were decapitated and placed on a bed of agarose/0.1× MMR, with an eye directed toward the light source. The electrode was then lowered onto the eye with a micromanipulator and inserted into the tissue to a depth of 100–150 µm, so that only the three or four lowest of the 16 electrodes of the linear array were, at any time, in electrical contact with the tissue, as evaluated by a visual inspection of electrode position and readout from the electrodes. The animals were briefly allowed to get used to the dark before stimulation (3 min). The stimulation consisted of 10-ms pulses of white light repeated 100 times at 1 Hz, triggered by a Digidata device (Axon; Molecular Devices). Signals were amplified with a 16-channel amplifier from Multi Channel Systems (model ME16-FAI-µPA-System), sampled at 10 kHz, and recorded with MC Rack software (Multi Channel Systems). Recordings were then transferred to Matlab (MathWorks) for further analysis with custom-designed scripts (see supplemental txt document code for analysis of ERG recordings).

Plots of a- and b-wave peak amplitudes as a function of stimulus intensity were well described by the Naka–Rushton function, a saturating nonlinearity of the form $V/V_{\max} = I^n/(I^n + I_{0.5}^n)$ (Naka and Rushton, 1966; Evans et al., 1993), where V is the wave peak amplitude, V_{\max} the saturating amplitude, n a dimensionless parameter, and $I_{0.5}$ is the stimulus intensity at half-saturating amplitude. Naka–Rushton parameters were estimated by fitting the equation $V/V_{\max} = I^n/(I^n + I_{0.5}^n)$, by a nonlinear least-squares method using GraphPad Prism (GraphPad Software).

Online supplemental material

Fig. S1 illustrates the effect of antisense MO oligonucleotides against USH1 gene transcripts in *X. tropicalis* larvae. Fig. S2 illustrates the effect of the coinjection of cRNAs coding for protocadherin-15 CD1 and CD3 isoforms together with the MO e6-i6 on the uptake of FM1-43 fluorescent dye by cranial neuromast hair cells in *X. tropicalis* larvae and shows the distribution of protocadherin-15 in the retinal photoreceptor cells. Fig. S3 illustrates the alterations of photoreceptor outer segments in *pcdh15* and *cdh23* morphants. Fig. S4 shows the normal distribution of peripherin and espin in photoreceptor cells of *pcdh15* morphant larvae. Fig. S5 illustrates the ultrastructure of photoreceptor outer segments in 3 and 4 dpf *pcdh15* morphant larvae. The Script.txt document includes the code used in Matlab (MathWorks) for analysis of ERG recordings.

Acknowledgments

We thank Jean-Pierre Hardelin for his significant contribution to the drafting of this manuscript; Laetitia Duhamel, Paul-Henri Prevot and Emilie Mace for assistance with ERG recordings and Matlab code; Eric Dufour and Senthil Arumugam for helpful discussions; and Albert Chesneau for assistance with *Xenopus* handling.

This work was supported by the FAUN Stiftung (Suchert Foundation), LHW-Stiftung, Retina France, the European Research Council advanced grant “Hair bundle” (ERC-2011-AdG 294570), the European Union Seventh Framework Program, under grant agreement HEALTH-F2-2010-242013 (TREATRUSH), the French Agence Nationale pour la Recherche as part of the second *Investissements d’Avenir* program (light4deaf, ANR-15-RHUS-0001), and the LabEx Lifesenses (ANR-10-LABX-65).

The authors declare no competing financial interests.

Author contributions: C. Petit and A. El-Amraoui conceived and supervised the study; C. Schietroma conceived and performed the experiments, analyzed the data, and interpreted the results; K. Parain and M. Perron assisted and provided critical expertise with animal husbandry and larval microinjections; A. Estivalet provided exper-

imental technical help; A. Aghaie generated the XPJM antibody; S. Picaud and J.-A. Sahel assisted with the electrophysiological recordings; and C. Schietroma, J. Boutet de Monvel, A. El-Amraoui, and C. Petit wrote, edited, and reviewed the manuscript.

Submitted: 6 December 2016

Revised: 26 February 2017

Accepted: 21 March 2017

References

- Adato, A., V. Michel, Y. Kikkawa, J. Reiners, K.N. Alagramam, D. Weil, H. Yonekawa, U. Wolfrum, A. El-Amraoui, and C. Petit. 2005. Interactions in the network of Usher syndrome type I proteins. *Hum. Mol. Genet.* 14:347–356. <http://dx.doi.org/10.1093/hmg/ddi031>
- Ahmed, Z.M., S. Riazuddin, S.L. Bernstein, Z. Ahmed, S. Khan, A.J. Griffith, R.J. Morell, T.B. Friedman, S. Riazuddin, and E.R. Wilcox. 2001. Mutations of the protocadherin gene *PCDH15* cause Usher syndrome type 1F. *Am. J. Hum. Genet.* 69:25–34. <http://dx.doi.org/10.1086/321277>
- Alagramam, K.N., H. Yuan, M.H. Kuehn, C.L. Murcia, S. Wayne, C.R.S. Srisailpathy, R.B. Lowry, R. Knaus, L. Van Laer, F.P. Bernier, et al. 2001. Mutations in the novel protocadherin *PCDH15* cause Usher syndrome type 1F. *Hum. Mol. Genet.* 10:1709–1718. (published erratum appears in *Hum. Mol. Genet.* 2001. 10:2603). <http://dx.doi.org/10.1093/hmg/10.16.1709>
- Alagramam, K.N., N.D. Miller, N.D. Adappa, D.R. Pitts, J.C. Heaphy, H. Yuan, and R.J. Smith. 2007. Promoter, alternative splice forms, and genomic structure of protocadherin 15. *Genomics*. 90:482–492. <http://dx.doi.org/10.1016/j.ygeno.2007.06.007>
- Bahloul, A., V. Michel, J.P. Hardelin, S. Nouaille, S. Hoos, A. Houdusse, P. England, and C. Petit. 2010. Cadherin-23, myosin VIIa and harmonin, encoded by Usher syndrome type I genes, form a ternary complex and interact with membrane phospholipids. *Hum. Mol. Genet.* 19:3557–3565. <http://dx.doi.org/10.1093/hmg/ddq271>
- Bibb, C., and R.W. Young. 1974. Renewal of fatty acids in the membranes of visual cell outer segments. *J. Cell Biol.* 61:327–343. <http://dx.doi.org/10.1083/jcb.61.2.327>
- Bitner-Blindziec, M., K.J. Lindley, P. Rutland, D. Blaydon, V.V. Smith, P.J. Milla, K. Hussain, J. Furth-Lavi, K.E. Cosgrove, R.M. Shepherd, et al. 2000. A recessive contiguous gene deletion causing infantile hyperinsulinism, enteropathy and deafness identifies the Usher type 1C gene. *Nat. Genet.* 26:56–60. <http://dx.doi.org/10.1038/79178>
- Boëda, B., A. El-Amraoui, A. Bahloul, R. Goodyear, L. Daviet, S. Blanchard, I. Perfettini, K.R. Fath, S. Shorte, J. Reiners, et al. 2002. Myosin VIIa, harmonin and cadherin 23, three Usher I gene products that cooperate to shape the sensory hair cell bundle. *EMBO J.* 21:6689–6699. <http://dx.doi.org/10.1093/emboj/cdf689>
- Boesze-Battaglia, K., and A.F. Goldberg. 2002. Photoreceptor renewal: A role for peripherin/rds. *Int. Rev. Cytol.* 217:183–225. [http://dx.doi.org/10.1016/S0074-7696\(02\)17015-X](http://dx.doi.org/10.1016/S0074-7696(02)17015-X)
- Bolz, H., B. von Brederlow, A. Ramírez, E.C. Bryda, K. Kutsche, H.G. Nothwang, M. Seeliger, M. del C-Salcedó Cabrera, M.C. Vila, O.P. Molina, et al. 2001. Mutation of *CDH23*, encoding a new member of the cadherin gene family, causes Usher syndrome type 1D. *Nat. Genet.* 27:108–112. <http://dx.doi.org/10.1038/83667>
- Bonilha, V.L., S.C. Finnemann, and E. Rodriguez-Boulan. 1999. Ezrin promotes morphogenesis of apical microvilli and basal infoldings in retinal pigment epithelium. *J. Cell Biol.* 147:1533–1548. <http://dx.doi.org/10.1083/jcb.147.7.1533>
- Bork, J.M., L.M. Peters, S. Riazuddin, S.L. Bernstein, Z.M. Ahmed, S.L. Ness, R. Polomeno, A. Ramesh, M. Schloss, C.R.S. Srisailpathy, et al. 2001. Usher syndrome 1D and nonsyndromic autosomal recessive deafness DFNB12 are caused by allelic mutations of the novel cadherin-like gene *CDH23*. *Am. J. Hum. Genet.* 68:26–37. <http://dx.doi.org/10.1086/316954>
- Caberlotto, E., V. Michel, J.B. de Monvel, and C. Petit. 2011. Coupling of the mechanotransduction machinery and stereocilia F-actin polymerization in the cochlear hair bundles. *BioArchitecture*. 1:169–174. <http://dx.doi.org/10.4161/bioa.1.4.17532>
- Chang, W.S., and W.A. Harris. 1998. Sequential genesis and determination of cone and rod photoreceptors in *Xenopus*. *J. Neurobiol.* 35:227–244. [http://dx.doi.org/10.1002/\(SICI\)1097-4695\(19980605\)35:3<227::AID-NEU1>3.0.CO;2-0](http://dx.doi.org/10.1002/(SICI)1097-4695(19980605)35:3<227::AID-NEU1>3.0.CO;2-0)

- Cohen, A.I. 1963. Vertebrate retinal cells and their organization. *Biol. Rev. Camb. Philos. Soc.* 38:427–459. <http://dx.doi.org/10.1111/j.1469-185X.1963.tb00789.x>
- Corless, J.M. 2012. Cone outer segments: a biophysical model of membrane dynamics, shape retention, and lamella formation. *Biophys. J.* 102:2697–2705. <http://dx.doi.org/10.1016/j.bpj.2012.04.052>
- Crawley, S.W., D.A. Shifrin Jr., N.E. Grega-Larson, R.E. McConnell, A.E. Benesh, S. Mao, Y. Zheng, Q.Y. Zheng, K.T. Nam, B.A. Millis, et al. 2014. Intestinal brush border assembly driven by protocadherin-based intermicrovillar adhesion. *Cell.* 157:433–446. <http://dx.doi.org/10.1016/j.cell.2014.01.067>
- Crawley, S.W., M.L. Weck, N.E. Grega-Larson, D.A. Shifrin Jr., and M.J. Tyska. 2016. ANKS4B is essential for intermicrovillar adhesion complex formation. *Dev. Cell.* 36:190–200. <http://dx.doi.org/10.1016/j.devcel.2015.12.022>
- Dong, W., R.H. Lee, H. Xu, S. Yang, K.G. Pratt, V. Cao, Y.K. Song, A. Nurmiikko, and C.D. Aizenman. 2009. Visual avoidance in *Xenopus* tadpoles is correlated with the maturation of visual responses in the optic tectum. *J. Neurophysiol.* 101:803–815. <http://dx.doi.org/10.1152/jn.90848.2008>
- Dosé, A.C., D.W. Hillman, C. Wong, L. Sohlberg, J. Lin-Jones, and B. Burnside. 2003. Myo3A, one of two class III myosin genes expressed in vertebrate retina, is localized to the calycal processes of rod and cone photoreceptors and is expressed in the sacculus. *Mol. Biol. Cell.* 14:1058–1073. <http://dx.doi.org/10.1091/mbc.E02-06-0317>
- Eckmiller, M.S. 1997. Morphogenesis and renewal of cone outer segments. *Prog. Retin. Eye Res.* 16:401–441. [http://dx.doi.org/10.1016/S1350-9462\(96\)00026-2](http://dx.doi.org/10.1016/S1350-9462(96)00026-2)
- Eckmiller, M.S. 2000. Microtubules in a rod-specific cytoskeleton associated with outer segment incisions. *Vis. Neurosci.* 17:711–722. <http://dx.doi.org/10.1017/S0952523800175054>
- Eckmiller, M.S. 2004. Defective cone photoreceptor cytoskeleton, alignment, feedback, and energetics can lead to energy depletion in macular degeneration. *Prog. Retin. Eye Res.* 23:495–522. <http://dx.doi.org/10.1016/j.preteyeres.2004.04.005>
- El-Amraoui, A., and C. Petit. 2014. The retinal phenotype of Usher syndrome: Pathophysiological insights from animal models. *C. R. Biol.* 337:167–177. <http://dx.doi.org/10.1016/j.crvi.2013.12.004>
- Evans, L.S., N.S. Peachey, and A.L. Marchese. 1993. Comparison of three methods of estimating the parameters of the Naka-Rushton equation. *Doc. Ophthalmol.* 84:19–30. <http://dx.doi.org/10.1007/BF01203279>
- Flores-Guevara, R., F. Renault, N. Loundon, S. Marlin, B. Pelosse, M. Momchilova, M. Auzoux-Chevé, A.I. Vermersch, and P. Richard. 2009. Usher syndrome type 1: Early detection of electroretinographic changes. *Eur. J. Paediatr. Neurol.* 13:505–507. <http://dx.doi.org/10.1016/j.ejpn.2008.10.002>
- Furness, D.N., and C.M. Hackney. 1985. Cross-links between stereocilia in the guinea pig cochlea. *Hear. Res.* 18:177–188. [http://dx.doi.org/10.1016/0378-5955\(85\)90010-3](http://dx.doi.org/10.1016/0378-5955(85)90010-3)
- Gale, J.E., W. Marcotti, H.J. Kennedy, C.J. Kros, and G.P. Richardson. 2001. FM1-43 dye behaves as a permeant blocker of the hair-cell mechano-transducer channel. *J. Neurosci.* 21:7013–7025.
- Germroth, P.G., R.G. Gourdie, and R.P. Thompson. 1995. Confocal microscopy of thick sections from acrylamide gel embedded embryos. *Microsc. Res. Tech.* 30:513–520. <http://dx.doi.org/10.1002/jemt.1070300608>
- Gillespie, P.G., and J.L. Cyr. 2004. Myosin-1c, the hair cell's adaptation motor. *Annu. Rev. Physiol.* 66:521–545. <http://dx.doi.org/10.1146/annurev.physiol.66.032102.112842>
- Goldberg, A.F. 2006. Role of peripherin/rds in vertebrate photoreceptor architecture and inherited retinal degenerations. *Int. Rev. Cytol.* 253:131–175. [http://dx.doi.org/10.1016/S0074-7696\(06\)53004-9](http://dx.doi.org/10.1016/S0074-7696(06)53004-9)
- Goodear, R.J., A. Forge, P.K. Legan, and G.P. Richardson. 2010. Asymmetric distribution of cadherin 23 and protocadherin 15 in the kinociliary links of avian sensory hair cells. *J. Comp. Neurol.* 518:4288–4297. <http://dx.doi.org/10.1002/cne.22456>
- Hanaichi, T., T. Sato, T. Iwamoto, J. Malavasi-Yamashiro, M. Hoshino, and N. Mizuno. 1986. A stable lead by modification of Sato's method. *J. Electron Microsc. (Tokyo).* 35:304–306.
- Hirsch, N., L.B. Zimmerman, and R.M. Grainger. 2002. *Xenopus*, the next generation: *X. tropicalis* genetics and genomics. *Dev. Dyn.* 225:422–433. <http://dx.doi.org/10.1002/dvdy.10178>
- Hollyfield, J.G., and P. Witkovsky. 1974. Pigmented retinal epithelium involvement in photoreceptor development and function. *J. Exp. Zool.* 189:357–377. <http://dx.doi.org/10.1002/jez.1401890309>
- Indzhukyan, A.A., R. Stepanyan, A. Nelina, K.J. Spinelli, Z.M. Ahmed, I.A. Belyantseva, T.B. Friedman, P.G. Barr-Gillespie, and G.I. Frolenkov. 2013. Molecular remodeling of tip links underlies mechanosensory regeneration in auditory hair cells. *PLoS Biol.* 11:e1001583. <http://dx.doi.org/10.1371/journal.pbio.1001583>
- James-Zorn, C., V.G. Ponferrada, K.A. Burns, J.D. Fortriede, V.S. Lotay, Y. Liu, J. Brad Karpinka, K. Karimi, A.M. Zorn, and P.D. Vize. 2015. Xenbase: Core features, data acquisition, and data processing. *Genesis.* 53:486–497. <http://dx.doi.org/10.1002/dvg.22873>
- Jaramillo, F., and A.J. Hudspeth. 1993. Displacement-clamp measurement of the forces exerted by gating springs in the hair bundle. *Proc. Natl. Acad. Sci. USA.* 90:1330–1334. <http://dx.doi.org/10.1073/pnas.90.4.1330>
- Kazmierczak, P., H. Sakaguchi, J. Tokita, E.M. Wilson-Kubalek, R.A. Milligan, U. Müller, and B. Kachar. 2007. Cadherin 23 and protocadherin 15 interact to form tip-link filaments in sensory hair cells. *Nature.* 449:87–91. <http://dx.doi.org/10.1038/nature06091>
- Lagziel, A., Z.M. Ahmed, J.M. Schultz, R.J. Morell, I.A. Belyantseva, and T.B. Friedman. 2005. Spatiotemporal pattern and isoforms of cadherin 23 in wild type and waltzer mice during inner ear hair cell development. *Dev. Biol.* 280:295–306. <http://dx.doi.org/10.1016/j.ydbio.2005.01.015>
- Larraín, J., M. Oelgeschläger, N.I. Kettura, B. Reversade, L. Zakin, and E.M. De Robertis. 2001. Proteolytic cleavage of Chordin as a switch for the dual activities of Twisted gastrulation in BMP signaling. *Development.* 128:4439–4447.
- Lefèvre, G., V. Michel, D. Weil, L. Lepelletier, E. Bizard, U. Wolfrum, J.P. Hardelin, and C. Petit. 2008. A core cochlear phenotype in USH1 mouse mutants implicates fibrous links of the hair bundle in its cohesion, orientation and differential growth. *Development.* 135:1427–1437. <http://dx.doi.org/10.1242/dev.012922>
- Maeda, R., K.S. Kindt, W. Mo, C.P. Morgan, T. Erickson, H. Zhao, R. Clemens-Grisham, P.G. Barr-Gillespie, and T. Nicolson. 2014. Tip-link protein protocadherin 15 interacts with transmembrane channel-like proteins TMC1 and TMC2. *Proc. Natl. Acad. Sci. USA.* 111:12907–12912. <http://dx.doi.org/10.1073/pnas.1402152111>
- Malm, E., V. Ponjavic, C. Möller, W.J. Kimberling, and S. Andréasson. 2011a. Phenotypes in defined genotypes including siblings with Usher syndrome. *Ophthalmic Genet.* 32:65–74. <http://dx.doi.org/10.3109/13816810.2010.536064>
- Malm, E., V. Ponjavic, C. Möller, W.J. Kimberling, E.S. Stone, and S. Andréasson. 2011b. Alteration of rod and cone function in children with Usher syndrome. *Eur. J. Ophthalmol.* 21:30–38. <http://dx.doi.org/10.5301/EJO.2010.5433>
- Marcy, Y., J. Prost, M.F. Carlier, and C. Sykes. 2004. Forces generated during actin-based propulsion: a direct measurement by micromanipulation. *Proc. Natl. Acad. Sci. USA.* 101:5992–5997. <http://dx.doi.org/10.1073/pnas.0307704101>
- Mathur, P., and J. Yang. 2015. Usher syndrome: Hearing loss, retinal degeneration and associated abnormalities. *Biochim. Biophys. Acta.* 1852:406–420. <http://dx.doi.org/10.1016/j.bbadi.2014.11.020>
- Michel, V., R.J. Goodyear, D. Weil, W. Marcotti, I. Perfettini, U. Wolfrum, C.J. Kros, G.P. Richardson, and C. Petit. 2005. Cadherin 23 is a component of the transient lateral links in the developing hair bundles of cochlear sensory cells. *Dev. Biol.* 280:281–294. <http://dx.doi.org/10.1016/j.ydbio.2005.01.014>
- Miloudi, C., F. Rossant, I. Bloch, C. Chaumette, A. Leseigneur, J.A. Sahel, S. Meimon, S. Mrejen, and M. Paques. 2015. The negative cone mosaic: a new manifestation of the optical Stiles-Crawford effect in normal eyes. *Invest. Ophthalmol. Vis. Sci.* 56:7043–7050. <http://dx.doi.org/10.1167/ivo.15-17022>
- Mollenhauer, H.H. 1964. Plastic embedding mixtures for use in electron microscopy. *Stain Technol.* 39:111–114.
- Moreau-Fauvarque, C., A. Kumanogoh, E. Camand, C. Jaillard, G. Barbin, I. Boquet, C. Love, E.Y. Jones, H. Kikutani, C. Lubetzki, et al. 2003. The transmembrane semaphorin Sema4D/CD100, an inhibitor of axonal growth, is expressed on oligodendrocytes and upregulated after CNS lesion. *J. Neurosci.* 23:9229–9239.
- Naka, K.I., and W.A. Rushton. 1966. An attempt to analyse colour reception by electrophysiology. *J. Physiol.* 185:556–586. <http://dx.doi.org/10.1111/j.1469-7758.1966.sp00802>
- Nawrot, M., K. West, J. Huang, D.E. Possin, A. Bretscher, J.W. Crabb, and J.C. Saari. 2004. Cellular retinaldehyde-binding protein interacts with ERM-binding phosphoprotein 50 in retinal pigment epithelium. *Invest. Ophthalmol. Vis. Sci.* 45:393–401. <http://dx.doi.org/10.1167/ivo.0393>
- Nieuwkoop, P.D., and J. Faber, editors. 1967. Normal Table of *Xenopus laevis* (Daudin): A Systematical and Chronological Survey of the Development from the Fertilized Egg till the End of Metamorphosis. North Holland Publishing Co., Amsterdam, the Netherlands. 252 pp.
- Pepermans, E., V. Michel, R. Goodyear, C. Bonnet, S. Abdi, T. Dupont, S. Gherbi, M. Holder, M. Makrelouf, J.P. Hardelin, et al. 2014. The CD2

- isoform of protocadherin-15 is an essential component of the tip-link complex in mature auditory hair cells. *EMBO Mol. Med.* 6:984–992. <http://dx.doi.org/10.15252/emmm.201403976>
- Prost, J., C. Barbetta, and J.F. Joanny. 2007. Dynamical control of the shape and size of stereocilia and microvilli. *Biophys. J.* 93:1124–1133. <http://dx.doi.org/10.1529/biophysj.106.098038>
- Ren, J., L. Wen, X. Gao, C. Jin, Y. Xue, and X. Yao. 2009. DOG 1.0: illustrator of protein domain structures. *Cell Res.* 19:271–273. <http://dx.doi.org/10.1038/cr.2009.6>
- Riazuddin, S., I.A. Belyantseva, A.P. Giese, K. Lee, A.A. Indzhykulian, S.P. Nandamuri, R. Yousaf, G.P. Sinha, S. Lee, D. Terrell, et al. 2012. Alterations of the CIB2 calcium- and integrin-binding protein cause Usher syndrome type IJ and nonsyndromic deafness DFNB48. *Nat. Genet.* 44:1265–1271. <http://dx.doi.org/10.1038/ng.2426>
- Richardson, G.P., J.B. de Monvel, and C. Petit. 2011. How the genetics of deafness illuminates auditory physiology. *Annu. Rev. Physiol.* 73:311–334. <http://dx.doi.org/10.1146/annurev-physiol-012110-142228>
- Safieddine, S., A. El-Amraoui, and C. Petit. 2012. The auditory hair cell ribbon synapse: From assembly to function. *Annu. Rev. Neurosci.* 35:509–528. <http://dx.doi.org/10.1146/annurev-neuro-061010-113705>
- Sahly, I., E. Dufour, C. Schietroma, V. Michel, A. Bahloul, I. Perfettini, E. Pepermans, A. Estivale, D. Carette, A. Aghaie, et al. 2012. Localization of Usher 1 proteins to the photoreceptor calyceal processes, which are absent from mice. *J. Cell Biol.* 199:381–399. <http://dx.doi.org/10.1083/jcb.201202012>
- Seiler, C., K.C. Finger-Baier, O. Rinner, Y.V. Makhankov, H. Schwarz, S.C. Neuhauss, and T. Nicolson. 2005. Duplicated genes with split functions: Independent roles of protocadherin15 orthologues in zebrafish hearing and vision. *Development.* 132:615–623. <http://dx.doi.org/10.1242/dev.01591>
- Siemens, J., P. Kazmierczak, A. Reynolds, M. Sticker, A. Littlewood-Evans, and U. Müller. 2002. The Usher syndrome proteins cadherin 23 and harmonin form a complex by means of PDZ-domain interactions. *Proc. Natl. Acad. Sci. USA.* 99:14946–14951. <http://dx.doi.org/10.1073/pnas.232579599>
- Šindelka, R., Z. Ferjentsik, and J. Jonák. 2006. Developmental expression profiles of *Xenopus laevis* reference genes. *Dev. Dyn.* 235:754–758. <http://dx.doi.org/10.1002/dvdy.20665>
- Sjöstrand, F.S., and L.G. Elfvin. 1957. Some observations on the structure of the retinal receptors of the toad eye as revealed by the electron microscope. In *Electron Microscopy: Proceedings of the Stockholm Conference, September, 1956*. F.S. Sjöstrand and J. Rhodin, editors. Academic Press, New York. 194–234.
- Söllner, C., G.J. Rauch, J. Siemens, R. Geisler, S.C. Schuster, U. Müller, T. Nicolson; Tübingen 2000 Screen Consortium. 2004. Mutations in cadherin 23 affect tip links in zebrafish sensory hair cells. *Nature.* 428:955–959. <http://dx.doi.org/10.1038/nature02484>
- Sotomayor, M., W.A. Weihofen, R. Gaudet, and D.P. Corey. 2012. Structure of a force-conveying cadherin bond essential for inner-ear mechanotransduction. *Nature.* 492:128–132. <http://dx.doi.org/10.1038/nature11590>
- Steinberg, R.H., S.K. Fisher, and D.H. Anderson. 1980. Disc morphogenesis in vertebrate photoreceptors. *J. Comp. Neurol.* 190:501–518. <http://dx.doi.org/10.1002/cne.901900307>
- Stiemke, M.M., R.A. Landers, M.R. al-Ubaidi, M.E. Rayborn, and J.G. Hollyfield. 1994. Photoreceptor outer segment development in *Xenopus laevis*: influence of the pigment epithelium. *Dev. Biol.* 162:169–180. <http://dx.doi.org/10.1006/dbio.1994.1076>
- Stuck, M.W., S.M. Conley, and M.I. Naash. 2016. PRPH2/RDS and ROM-1: Historical context, current views and future considerations. *Prog. Retin. Eye Res.* 52:47–63. <http://dx.doi.org/10.1016/j.preteyeres.2015.12.002>
- Szikra, T., S. Trenholm, A. Drinnenberg, J. Jüttner, Z. Raics, K. Farrow, M. Biel, G. Awatramani, D.A. Clark, J.A. Sahel, et al. 2014. Rods in daylight act as relay cells for cone-driven horizontal cell-mediated surround inhibition. *Nat. Neurosci.* 17:1728–1735. <http://dx.doi.org/10.1038/nn.3852>
- Takahashi, S., V.J. Mui, S.K. Rosenberg, K. Homma, M.A. Cheatham, and J. Zheng. 2016. Cadherin 23-C regulates microtubule networks by modifying CAMSAP3's function. *Sci. Rep.* 6:28706. <http://dx.doi.org/10.1038/srep28706>
- Verpy, E., M. Leibovici, I. Zwaenepoel, X.-Z. Liu, A. Gal, N. Salem, A. Mansour, S. Blanchard, I. Kobayashi, B.J.B. Keats, et al. 2000. A defect in harmonin, a PDZ domain-containing protein expressed in the inner ear sensory hair cells, underlies Usher syndrome type 1C. *Nat. Genet.* 26:51–55. <http://dx.doi.org/10.1038/79171>
- Volland, S., L.C. Hughes, C. Kong, B.L. Burgess, K.A. Linberg, G. Luna, Z.H. Zhou, S.K. Fisher, and D.S. Williams. 2015. Three-dimensional organization of nascent rod outer segment disk membranes. *Proc. Natl. Acad. Sci. USA.* 112:14870–14875. <http://dx.doi.org/10.1073/pnas.1516309112>
- Weil, D., A. El-Amraoui, S. Masmoudi, M. Mustapha, Y. Kikkawa, S. Lainé, S. Delmaghani, A. Adato, S. Nadifi, Z.B. Zina, et al. 2003. Usher syndrome type I G (USH1G) is caused by mutations in the gene encoding SANS, a protein that associates with the USH1C protein, harmonin. *Hum. Mol. Genet.* 12:463–471. <http://dx.doi.org/10.1093/hmg/ddg051>
- Well, D., S. Blanchard, J. Kaplan, P. Guilford, F. Gibson, J. Walsh, P. Mburu, A. Varela, J. Levilliers, M.D. Weston, et al. 1995. Defective myosin VIIA gene responsible for Usher syndrome type 1B. *Nature.* 374:60–61. <http://dx.doi.org/10.1038/374060a0>
- Williams, D.S. 2008. Usher syndrome: Animal models, retinal function of Usher proteins, and prospects for gene therapy. *Vision Res.* 48:433–441. <http://dx.doi.org/10.1016/j.visres.2007.08.015>
- Wilson, J.M., R.M. Bunte, and A.J. Cartt. 2009. Evaluation of rapid cooling and tricaine methanesulfonate (MS222) as methods of euthanasia in zebrafish (*Danio rerio*). *J. Am. Assoc. Lab. Anim. Sci.* 48:785–789.
- Witkovsky, P. 2000. Photoreceptor classes and transmission at the photoreceptor synapse in the retina of the clawed frog, *Xenopus laevis*. *Microsc. Res. Tech.* 50:338–346. [http://dx.doi.org/10.1002/1097-0029\(20000901\)50:5<338::AID-JEMT3>3.0.CO;2-I](http://dx.doi.org/10.1002/1097-0029(20000901)50:5<338::AID-JEMT3>3.0.CO;2-I)
- Young, R.W. 1967. The renewal of photoreceptor cell outer segments. *J. Cell Biol.* 33:61–72. <http://dx.doi.org/10.1083/jcb.33.1.61>